Cell Reports
Methods

Article

Rapid manipulation of mitochondrial morphology in a living cell with iCMM

Graphical abstract

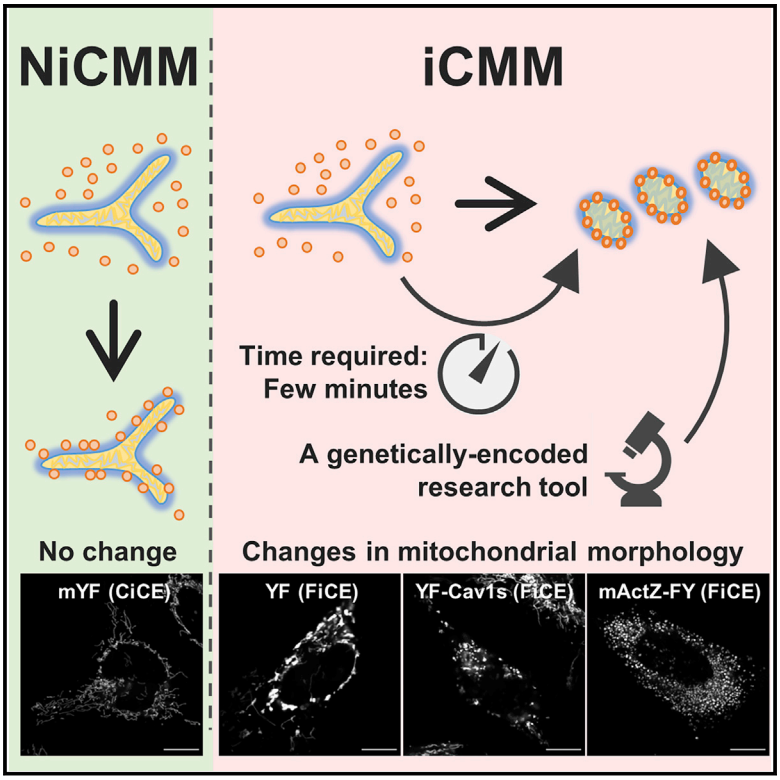

Highlights

- iCMM can induce mitochondrial morphological changes on the minute timescale
- We develop three iCMM effectors that can alter mitochondrial morphology
- iCMM alters mitochondrial morphology with a negligible effect on membrane potential

Authors

Takafumi Miyamoto, Hideki Uosaki, Yuhei Mizunoe, ..., Naoya Yahagi, Koichi Ito, Hitoshi Shimano

Correspondence

takmi565@md.tsukuba.ac.jp

In brief

The biological significance of mitochondrial morphology in human health and diseases is not fully elucidated. Miyamoto et al. develop iCMM, a genetically encoded synthetic protein device, to alter mitochondrial morphology on a minute timescale and describe the effects of iCMM-induced mitochondrial morphological changes in living cells.

Miyamoto et al., 2021, Cell Reports Methods *1*, 100052
August 23, 2021
https://doi.org/10.1016/j.crmeth.2021.100052

CellPress

Cell Reports Methods

CellPress
OPEN ACCESS

Article

Rapid manipulation of mitochondrial morphology in a living cell with iCMM

Takafumi Miyamoto,[1,9,10,*] Hideki Uosaki,[2] Yuhei Mizunoe,[1] Song-Iee Han,[1] Satoi Goto,[1] Daisuke Yamanaka,[3] Masato Masuda,[4] Yosuke Yoneyama,[5] Hideki Nakamura,[6,7] Naoko Hattori,[8] Yoshinori Takeuchi,[1] Hiroshi Ohno,[1] Motohiro Sekiya,[1] Takashi Matsuzaka,[1] Fumihiko Hakuno,[4] Shin-Ichiro Takahashi,[4] Naoya Yahagi,[1] Koichi Ito,[3] and Hitoshi Shimano[1]

[1]Department of Internal Medicine (Endocrinology and Metabolism), Faculty of Medicine, University of Tsukuba, Tsukuba, Ibaraki 305-8575, Japan
[2]Division of Regenerative Medicine, Center for Molecular Medicine, Jichi Medical University, Shimotsuke, Tochigi 329-0498, Japan
[3]Department of Veterinary Medical Sciences, Graduate School of Agriculture and Life Sciences, The University of Tokyo, Kasama, Ibaraki 319-0206, Japan
[4]Departments of Animal Sciences and Applied Biological Chemistry, Graduate School of Agriculture and Life Sciences, The University of Tokyo, Bunkyo-ku, Tokyo 113-8657, Japan
[5]Institute of Research, Division of Advanced Research, Tokyo Medical and Dental University (TMDU), Bunkyo-ku, Tokyo 113-8510, Japan
[6]Johns Hopkins University School of Medicine, Department of Cell Biology and Center for Cell Dynamics, MD 21205, USA
[7]Kyoto University Graduate School of Engineering, Department of Synthetic Chemistry and Biological Chemistry, Graduate School of Engineering, Kyoto University, Kyoto, Kyoto 606-8501, Japan
[8]Division of Epigenomics, National Cancer Center Research Institute, Chuo-ku, Tokyo 104-0045, Japan
[9]Transborder Medical Research Center, University of Tsukuba, Tsukuba, Ibaraki 305-8577, Japan
[10]Lead contact
*Correspondence: takmi565@md.tsukuba.ac.jp
https://doi.org/10.1016/j.crmeth.2021.100052

MOTIVATION Mitochondria exhibit a variety of morphologies depending on the physiopathological condition of the cell, but the significance of changes in mitochondrial morphology remains almost unresolved. Although a method to induce mitochondrial morphological changes by altering the expression of proteins involved in mitochondrial dynamics has been established, this method requires several hours or more to induce mitochondrial morphological changes. Accordingly, a method to induce mitochondrial morphological changes at any given point in time on a minute timescale is needed.

SUMMARY

Engineered synthetic biomolecular devices that integrate elaborate information processing and precisely regulate living cell behavior have potential in various applications. Although devices that directly regulate key biomolecules constituting inherent biological systems exist, no devices have been developed to control intracellular membrane architecture, contributing to the spatiotemporal functions of these biomolecules. This study developed a synthetic biomolecular device, termed inducible counter mitochondrial morphology (iCMM), to manipulate mitochondrial morphology, an emerging informative property for understanding physiopathological cellular behaviors, on a minute timescale by using a chemically inducible dimerization system. Using iCMM, we determined cellular changes by altering mitochondrial morphology in an unprecedented manner. This approach serves as a platform for developing more sophisticated synthetic biomolecular devices to regulate biological systems by extending manipulation targets from conventional biomolecules to mitochondria. Furthermore, iCMM might serve as a tool for uncovering the biological significance of mitochondrial morphology in various physiopathological cellular processes.

INTRODUCTION

A fascinating advance in the field of synthetic biology, in which biological functions that do not exist in nature are engineered, is the creation of synthetic biomolecular devices to manipulate living cells at will (Grozinger et al., 2019; Khalil and Collins, 2010). Indeed, with the advent of more sophisticated biological tools, both nucleic acid- and protein-based synthetic biomolecular devices to control cellular functions have been generated and are being applied to clinical medicine and other fields

(Clarke and Kitney, 2020; Folcher and Fussenegger, 2012). In general, these synthetic biomolecular devices regulate cellular functions by manipulating the expression levels, localization, and activities of key responsible biomolecules. However, organelle morphology, which also plays a critical role in the spatiotemporal regulation of biomolecule functions and subsequent execution of cellular functions, remains virtually unexplored as a target for synthetic biomolecular devices because of the paucity of applicable techniques. Meanwhile, concomitant with recent research, there is increasing interest in organelle morphology, which contributes to versatile physiopathological cellular behaviors that have not generally been thought to involve organelle morphology (Archer, 2013; Lomakin et al., 2020; Tao et al., 2020; Venturini et al., 2020). One of these organelles is the mitochondrion.

Mitochondria are organelles in eukaryotic cells that evolved from endosymbiotic α-proteobacteria (Gray et al., 2001). They are involved in numerous anabolic and catabolic reactions, including but not limited to oxidative phosphorylation, the tricarboxylic acid cycle, the β-oxidation of fatty acids, and heme biosynthesis (Smeitink et al., 2006). The products of these reactions are used in various cellular processes, including cellular structuring, chemical reactions, and signal transduction, indicating that mitochondria are unequivocally indispensable to host cells.

As their name implies (from Greek: mitos = thread; chondrion = granule), mitochondria are highly dynamic organelles that can alter their size, shape, and subcellular distribution through repetitive, coordinated fusion and fission cycles over the course of a few minutes (Detmer and Chan, 2007; Jakobs et al., 2003), a phenomenon termed mitochondrial dynamics. Accumulating evidence has revealed that disturbances in mitochondrial dynamics followed by the disruption of mitochondrial morphology occur in various diseases, including cancer and metabolic diseases (Archer, 2013; Yu-Wai-Man and Chinnery, 2012), leading to an increasing appreciation of the pivotal role of mitochondrial morphology in physiopathological cellular behaviors. However, the disorganization of mitochondrial morphology is just now emerging as a mechanism of these cellular behaviors; the biological significance of mitochondrial morphology in health and disease remains to be completely elucidated.

Over recent decades, considerable efforts have been made to elucidate the physiopathological significance of mitochondrial morphology. In most of these studies, mitochondrial morphology has been altered either chemically or by modifying genes (Cassidy-Stone et al., 2008; Leonard et al., 2015; Picard et al., 2013). However, as these approaches have caused concomitant mitochondrial dysfunction, whether subsequent cell changes are due to mitochondrial morphology changes, mitochondrial dysfunction, or both remains to be clarified. Thus, a tool for the inducible, rapid, and specific manipulation of mitochondrial morphology without abrogating mitochondrial functions is required (Picard et al., 2013; Wai and Langer, 2016). Furthermore, if this tool allows us to reorganize intracellular status as intended through the rapid manipulation of mitochondrial morphology, the mitochondrion would be a promising target for synthetic biomolecular devices.

Chemically inducible dimerization (CID) systems allow manipulating target protein localization in a spatiotemporally confined subcellular compartment by forming a small molecule-induced ternary complex of two different proteins (Derose et al., 2013). Notably, CID systems are applied to synthetic biomolecular devices to control cellular outputs by spatiotemporally regulating protein functions (Fegan et al., 2010; Miyamoto et al., 2013; Putyrski and Schultz, 2012). Compared with the hours-long genetic circuit-based manipulation of cellular outputs, CID systems allow for faster control of cellular outputs (seconds to minutes) (Miyamoto et al., 2012). Therefore, they are suitable for rapidly inducing morphological changes in mitochondria at a specific time point. CID systems have been widely applied in mitochondrial studies, for example, to promote the mitochondria-endoplasmic reticulum (ER) interaction (Csordás et al., 2010) and to suppress AMP-activated protein kinase activity in mitochondria (Miyamoto et al., 2015). However, a sophisticated platform for manipulating mitochondrial morphology into various patterns using CID systems is lacking.

In the present study, we developed inducible counter mitochondrial morphology (iCMM), a CID system-based synthetic protein device, to manipulate mitochondrial morphology in living cells on a minute timescale. Using iCMM, we determined the type of alterations that occur immediately after morphological changes, which would otherwise be difficult to study. This study illustrates that iCMM is a potentially powerful tool that, in addition to conventional methods, can reveal the biological significance of mitochondrial morphology in various physiopathological cellular behaviors. Furthermore, the iCMM-induced perturbation of mitochondrial morphology evokes reorganization of the intracellular transcriptome and amino acid profile, suggesting that it could help regulate cells as intended. Expanding the target of manipulation by synthetic devices from biomolecules to mitochondria is promising for developing more proficient strategies to control cellular functions in various applications.

RESULTS

Development of a genetically encoded synthetic protein device: iCMM

iCMM, a Boolean YES logic gate-based synthetic protein device, consists of a functional iCMM effector (FiCE) to perturb mitochondrial morphology and a mitochondrial outer membrane-specific anchor protein that tethers the effector to the mitochondria in the presence of a chemical dimerizer (Figure 1A). Considering the versatility and translocation speed of effector proteins, we adopted a rapamycin-based CID system, in which peptidyl-prolyl *cis-trans* isomerase FKBP12 (termed FKBP) and the FKBP12-rapamycin-binding domain in the mammalian target of rapamycin (mTOR) (termed FRB) served as an effector and anchor, respectively, by using rapamycin as a chemical dimerizer (Figure 1B).

We first used a reported fundamental fusion protein consisting of enhanced yellow fluorescent protein (EYFP) and FKBP (termed YF) as a FiCE (Figure 1B). YF has been used as a control effector in various experimental settings (Inoue et al., 2005; Nakamura et al., 2020). However, we found that once it had substantially translocated to the outer surfaces of mitochondria, which were circumscribed by anchor proteins consisting of mitochondrial targeting sequences derived from Tom20, enhanced

CellPress
OPEN ACCESS

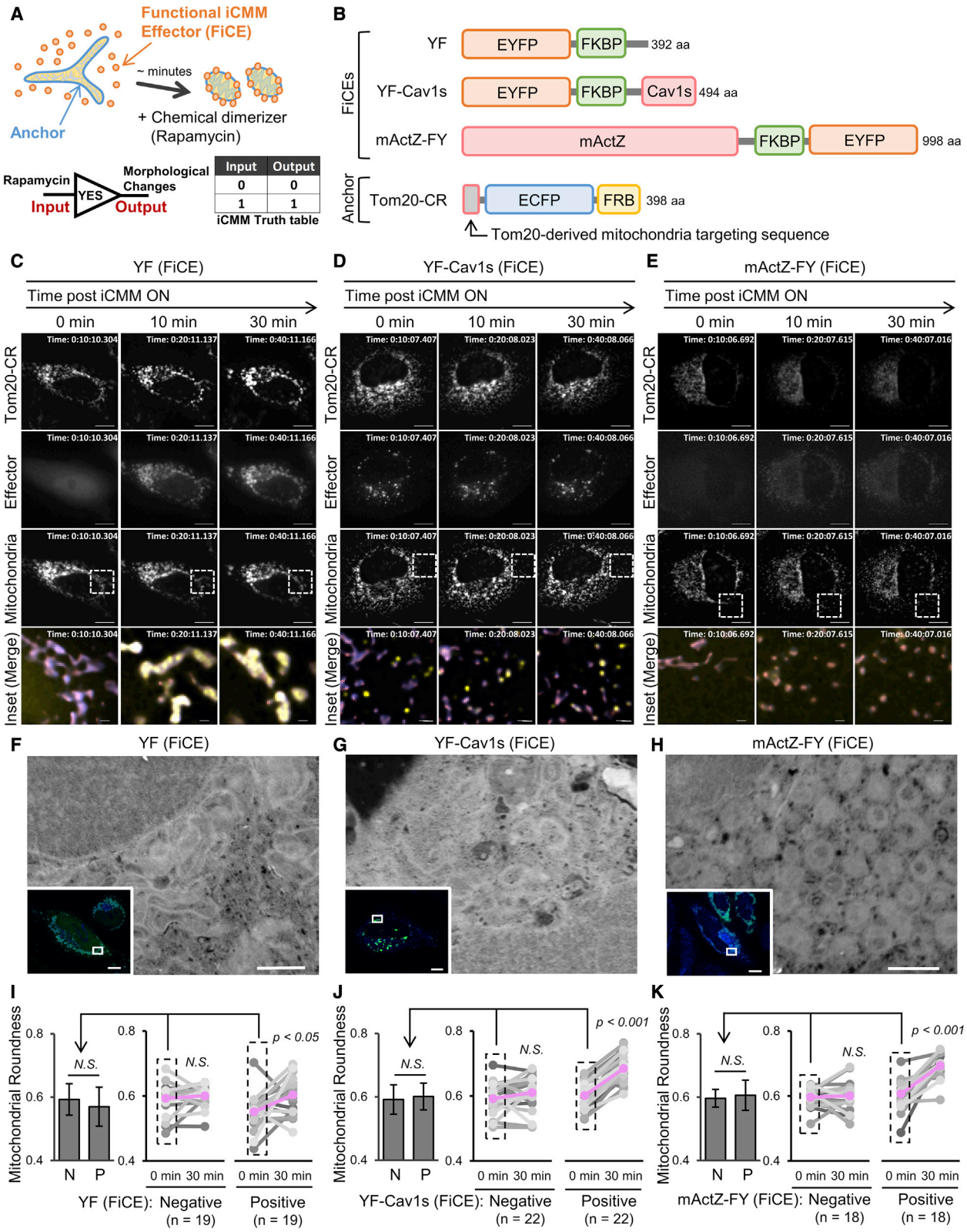

(legend on next page)

cyan fluorescent protein (ECFP), and FRB (termed Tom20-CR, Figure 1B), the mitochondrial morphology changed from a network structure to large punctate structures (Figures 1C, S1F, and Video S1). Correlative light and electron microscopy (CLEM) and confocal microscopy indicated that the large punctate structure of mitochondria induced by YF translocation was not a single mitochondrion but consisted of multiple mitochondria (Figures 1F and S2B). mYF containing monomeric EYFP^{A207K} (mEYFP) and FKBP (Figure S1A) did not change mitochondrial morphology, although mYF substantially accumulated in the mitochondrial outer membrane (Figures S1C, S1E, S2A, and Video S2), suggesting that the inherent homodimerization activity of EYFP (Lambert, 2019) was at least partially required for the YF-induced change in mitochondrial morphology. We used mYF as a control effector (CiCE) in subsequent experiments. In addition, we termed a synthetic protein device consisting of CiCE and a mitochondrial outer membrane-specific anchor protein (Tom20-CR, in this study) as Negative iCMM (NiCMM) (Figure S1B).

Excessive mitochondrial tethering with other membrane structures leads to the disruption of mitochondrial morphology (Kakimoto et al., 2018). Thus, we next focused on caveolin-1, an integral membrane protein that localizes to the caveola and multiple interior compartments through vesicle trafficking (Parton and Simons, 2007). As fluorescent protein-fused caveolin-1 exhibits a punctate distribution pattern in the cell similar to that of endogenous caveolin-1 (Schlegel and Lisanti, 2000), we hypothesized that tethering mitochondria to fluorescent protein-fused caveolin-1 via the CID system would induce a change in mitochondrial morphology. To test this idea, we constructed the second FiCE consisting of YF and amino acids (aa) 61–178 of caveolin-1 (termed YF-Cav1s; Figure 1B), the smallest fusion protein that showed a small punctate distribution pattern throughout the cell (Figure S3A). As expected, immunocytochemistry revealed that YF-Cav1s colocalized with endogenous caveolin-1 (Figure S3B). Most of the YF-Cav1s localized to certain regions within the cell and did not diffuse throughout the cell (Video S3). After the iCMM harboring YF-Cav1s was turned on, the mitochondrial surfaces were partially interlinked with YF-Cav1s, resulting in a change in mitochondrial morphology from a network structure to punctate structures of various sizes in the cells (Figures 1D, 1G, S1G, and S2C, and Video S4).

Finally, we optimized a previously designed interspecies fusion protein consisting of amino acids 30–262 of *Listeria monocytogenes* actin assembly inducing protein (ActA) that was codon-optimized for usage in mammalian cells (Nakamura et al., 2020) and amino acids 2–380 of human zyxin (termed mActZ), which is structurally and functionally similar to full-length ActA (Golsteyn et al., 1997). As ActA converts actin polymerization into a motile force (Smith and Portnoy, 1997), we hypothesized that the generated propulsive force could alter mitochondrial morphology. mActZ was fused to FKBP and EYFP (termed mActZ-FY; Figure 1B) to produce the third FiCE. Similar to the mitochondrial morphology induced by ActuAtor (a fusion protein consisting of codon-optimized ActA, FKBP, and mCherry), a protein functionally homologous to mActZ-FY, when iCMM harboring mActZ-FY were turned on, cytoplasmic mActZ-FY was recruited to the mitochondria, and then the morphology of mitochondria rapidly and obviously changed to small dot-like structures (Figures 1E, 1H, S1H, and S2D, and Video S5). Of note, the expression level of mActZ-FY was lower than that of the other FiCEs, probably due to the instability of mActZ-FY, but significant changes in mitochondrial morphology were observed after the translocation of mActZ-FY in mitochondria.

Together, these results indicate that each of the three FiCEs developed here can induce characteristic changes in mitochondrial morphology at any given point in time on a minute timescale.

iCMM specifically alters mitochondrial morphology in target cells

In addition to the timescale, properties that allow us to induce mitochondrial morphological changes in only target cells in a switch-dependent manner are also important for iCMM. Because changes in mitochondrial morphology caused by iCMM resulted in the loss of a mitochondrial thread-like structure (Figures 1C–1E), the effect of iCMM was assessed by the roundness of the mitochondria. As expected, disruption of mitochondrial morphology was observed only in cells expressing iCMM, not in those expressing NiCMM or in peripheral non-iCMM-expressing cells, indicating that iCMM induced mitochondrial morphological changes in only the target cells (Figures 1I–1K and S1D). We further confirmed that iCMM-induced morphological changes in the mitochondria are independent of DRP1, a protein that regulates mitochondrial fission (Figure 2).

We next examined whether iCMM can specifically induce mitochondrial morphology changes without altering the morphology of other organelles. Time-lapse imaging revealed that the FiCEs accumulated in mitochondria only after the device

Figure 1. iCMM as a synthetic protein device for rapid manipulation of mitochondrial morphology in live cells

(A) Schematic diagram of the iCMM system.

(B) Structural features of FiCEs and anchor.

(C–E) Time-lapse imaging (2 min/frame) of HeLa cells expressing Tom20-CR (slate blue) and the indicated effectors (yellow). Mitochondria (coral) were stained with the MitoTracker Red CMXRos dye. Rapamycin (50 nM) was added after image acquisition at frame 6 (indicated as "0 min"). Scale bar : 10 μm. Insets show a magnified view of the boxed area. Scale bar in inset, 1 μm. Lookup tables (LUTs) (effector): 100–2,000, YF (C) and YF-Cav1s (D); 100–500, mActZ-FY (E).

(F–H) Mitochondrial structures in HeLa cells expressing the indicated effectors and Tom20-CR were examined with CLEM after 30 min of iCMM actuation (50 nM rapamycin addition). Merged fluorescence images (blue, Tom20-CR; green, indicated effector, inset) and SEM images are shown. Scale bar, 10 μm in insets and 1 μm in SEM images.

(I–K) Mitochondrial roundness in HeLa cells expressing indicated iCMM (positive, P) and in peripheral iCMM-negative cells ([negative, N) were analyzed before (0 min) and after (30 min) activation of the iCMM system (50 nM rapamycin addition). (Left) Data represent mean ± standard deviation. N.S., statistically non-significant (Student's t test); (right) gray, analyzed single cell; lavender, average. n = number of cells analyzed, from three independent experiments. p = paired t test. N.S., statistically non-significant. See also Figures S1–S5 and S9, and Videos S1, S3, S4, and S5.

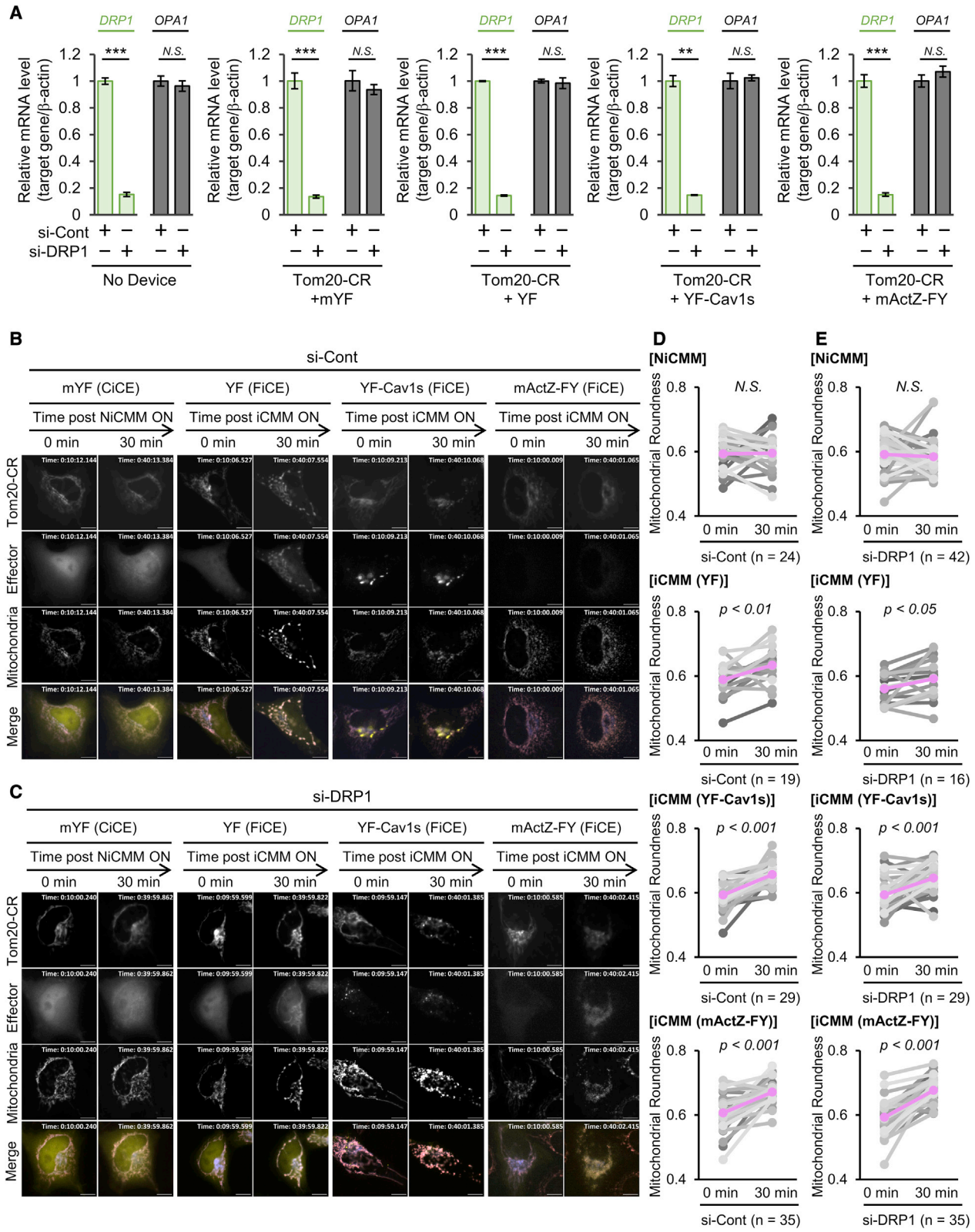

(legend on next page)

had been turned on and thus did not induce morphological changes in ER, Golgi apparatus, and lysosomes over a 120-min observation window (Figure S4).

One of the CID system's strengths is its versatility (Miyamoto et al., 2013). To determine its versatility, iCMM was transduced into Hep 3B human liver cancer cells and U-2 OS (human osteosarcoma) cells. Consistent with the results obtained from HeLa human ovarian cancer cells (Figure 1), each FiCE induced a characteristic change in mitochondrial morphology in both cell types on similar timescales (Figure S5).

Together, these results indicate that iCMM is a powerful tool for specifically disrupting mitochondrial morphology in target cells.

iCMM alters mitochondrial morphology without loss of mitochondrial membrane potential

The mitochondrial membrane potential (MMP), which results from redox transformations, plays decisive roles in various cellular functions, including adenosine triphosphate (ATP) synthesis and innate immune responses (Ichinohe et al., 2013; Koshiba et al., 2011; Zorova et al., 2018). Remarkably, MMP loss is a major factor in the disintegration of mitochondrial morphology (Zhang et al., 2014). Thus, we examined whether iCMM-induced morphological changes in mitochondria were attributable to a loss of MMP by using tetramethylrhodamine ethyl ester (TMRE). Although TMRE is appreciated as a useful MMP indicator, it is also recognized as a potent photosensitizer that can cause mitochondrial damage by sequential fluorescent illumination (Hsieh et al., 2015; Yang and Yang, 2011). Thus, to measure MMP, the TMRE fluorescence intensity was assessed at each time point instead of prolonged time-lapse imaging. We found that, regardless of the FiCE used, the MMP did not change before or after the change in mitochondrial morphology caused by iCMM over a 120-min time window (Figures 3A–3D). These results suggest that iCMM induces mitochondrial morphological changes irrespective of MMP and also indicates that such changes do not cause a loss of MMP under the experimental conditions.

We next examined whether changes in mitochondrial morphology induced by iCMM altered the susceptibility of mitochondria to carbonyl cyanide 4- (trifluoromethoxy) phenylhydrazone (FCCP), an ionophore uncoupler of oxidative phosphorylation (Figure 3I, left). Time-lapse imaging revealed that FCCP treatment resulted in a comparable loss of MMP irrespective of mitochondrial morphology (Figures 3E–3I). Together, these results indicate that iCMM alters mitochondrial morphology with a negligible effect on MMP.

We further confirmed that iCMM-induced mitochondrial morphological changes did not promote reactive oxygen species (ROS) production in mitochondria as measured by MitoSOX (Figure 4).

Disruption of mitochondrial morphology by mActZ-FY, but not other effectors, suppresses oxygen consumption by mitochondria

In mammalian cells, mitochondria are responsible for the majority of cellular oxygen consumption to generate ATP. To maintain bioenergetic activity in this process, mitochondria go through repeated fusion and fission cycles (Chen et al., 2005; Rapaport et al., 1998; Twig et al., 2008). To examine iCMM-induced mitochondrial morphology disruption on mitochondrial respiration capacity, we established cell lines stably expressing iCMM. Compared with control cells that stably expressed NiCMM (NiCMM cells), cells stably expressing iCMM (iCMM^{YF}, iCMM^{Cav1s}, and iCMM^{mActZ}, respectively) showed no noticeable difference in cell proliferation or cell morphology (Figures S6A and S6B). As expected, cells stably expressing iCMM, not NiCMM, showed mitochondrial morphological changes in a switch-dependent manner, as were cells transiently expressing iCMM (Figure S6C).

We then examined mitochondrial respiration activity in cells stably expressing iCMM by measuring the oxygen consumption rate (OCR). Before OCR measurements, cells were treated with rapamycin to actuate iCMM/NiCMM or with DMSO as a counterpart for 30 or 120 min. Although rapamycin can affect the OCR under certain conditions (Lerner et al., 2013; Rosario et al., 2019), no significant difference in OCR was observed between NiCMM cells treated with DMSO and those treated with rapamycin, indicating that rapamycin, at least under the experimental conditions (50 nM, a 120-min time window), did not affect the OCR (Figures 5A and S6D). Similarly, disruption of mitochondrial morphology by YF and YF-Cav1s did not affect the OCR over a 120-min time window (Figures 5B, 5C, S6E, and S6F), indicating that YF and YF-Cav1s could induce changes in mitochondrial morphology without altering the OCR. In contrast, induction of mitochondrial morphological changes by mActZ-FY resulted in a significant decrease in OCR within 30 min (Figures 5D and S6G). Of note, there was no statistically significant difference in the maximum OCR in iCMM^{mActZ} cells at 120 min, but the maximum OCR exhibited a downward trend when the iCMM harboring mActZ-FY was turned on (Figure S6G). We also found that disruption of mitochondrial morphology by mActZ-FY reduced the basal extracellular acidification rate (ECAR), an indicator of glycolysis, at 120 min, but the difference at 30 min was

Figure 2. iCMM could induce changes in mitochondrial morphology in a DRP1-independent manner

(A) Twenty-four hours after transfection of the indicated small interfering RNA (siRNA), HeLa cells were transfected with the indicated plasmids required for the NiCMM/iCMM system. Eighteen hours later, the mRNA expression level of *DRP1* and *OPA1* was determined by quantitative polymerase chain reaction (PCR) (ΔΔCt method). The data are presented as the mean ± standard deviation from three independent experiments. **p < 0.01, ***p < 0.001, N.S., statistically non-significant (Student's t test).

(B and C) Representative time-lapse images (5 min/frame) of si-Cont-transfected HeLa cells (B) and *DRP1*-knockdown HeLa cells (C) transiently expressing Tom20-CR (slate blue) and the indicated effector (yellow). Cells were prepared as in (A). Rapamycin (50 nM) was added after image acquisition at frame 3 (indicated as 0 min). Mitochondria (coral) were stained with the MitoTracker Red CMXRos dye. Scale bar, 10 μm. si-Cont LUTs (effector): 100–1,600, (mYF, YF, and YF-Cav1s), 120–500 (mActZ-FY). si-DRP1 LUTs (effector): 100–800 (mYF, YF, and YF-Cav1s), 100–300 (mActZ-FY).

(D and E) Mitochondrial roundness in indicated HeLa cells si-Cont (D) and si-DRP1 (E) were analyzed before (0 min) and after (30 min) activation of the NiCMM/iCMM system (50 nM rapamycin addition). Gray, analyzed single cell; lavender, average. n = number of cells analyzed, from three independent experiments. p = paired t test. N.S., statistically non-significant.

CellPress
OPEN ACCESS

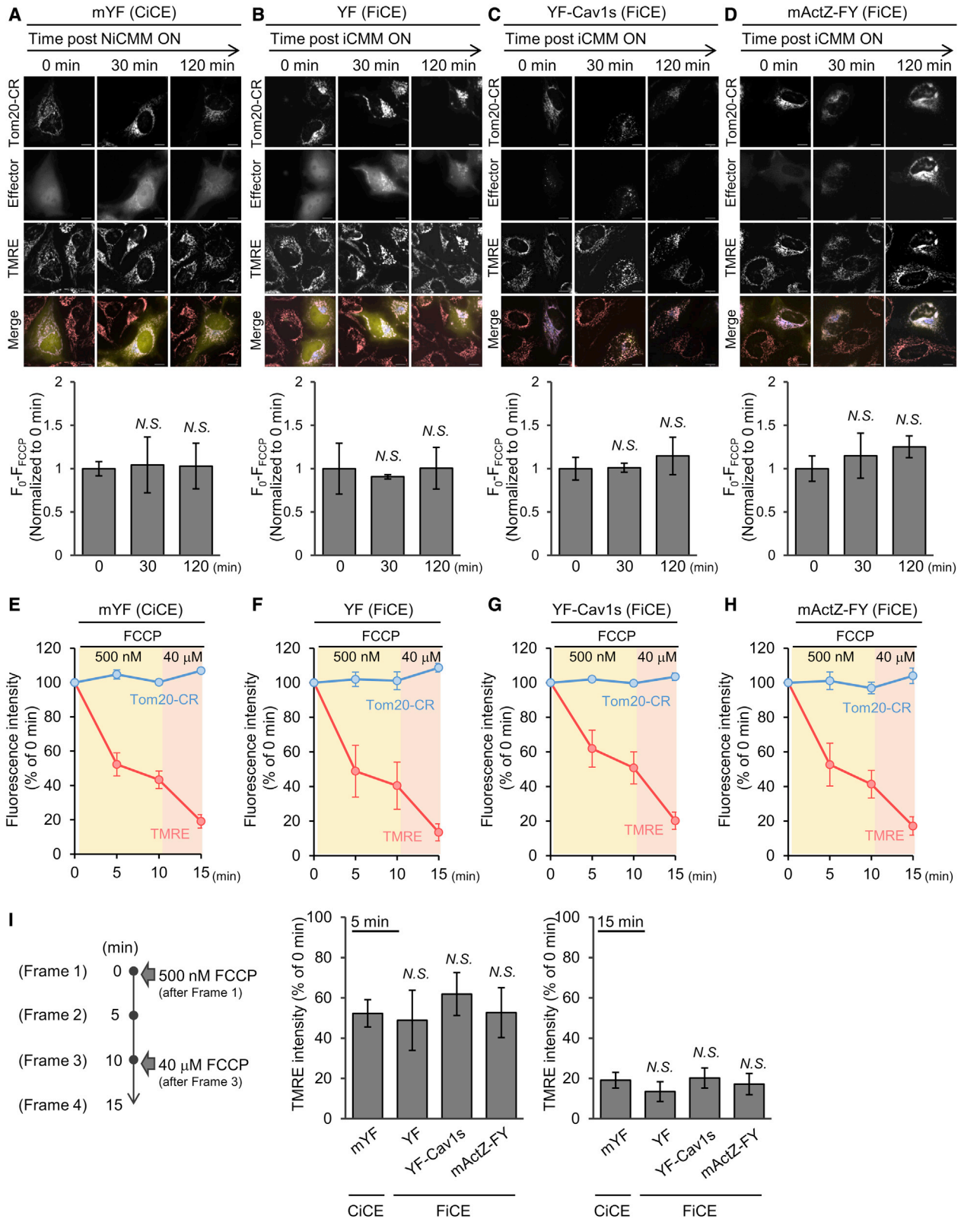

(legend on next page)

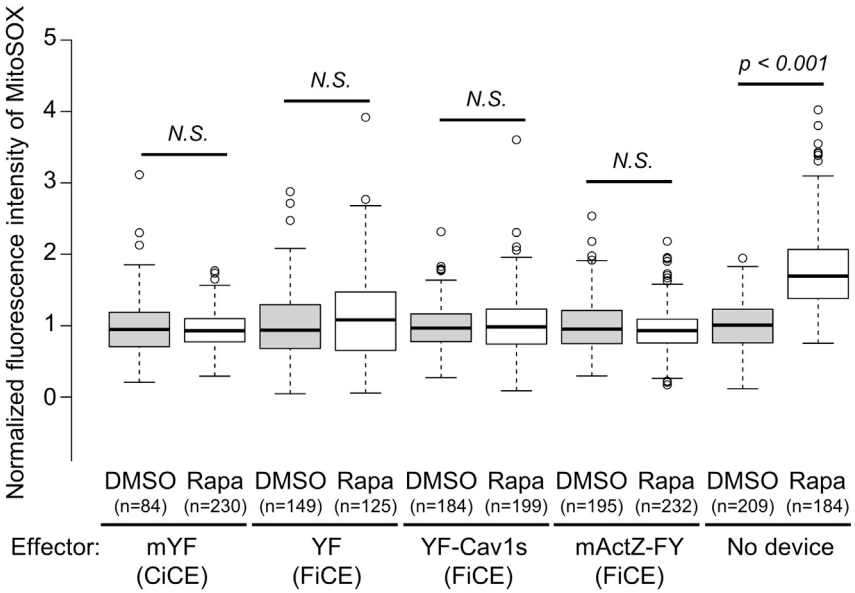

Figure 4. iCMM-induced changes in mitochondrial morphology do not increase mitochondrial ROS

HeLa cells transiently expressing Tom20-CR and the indicated effector were treated with either DMSO or 50 nM rapamycin for 2 h. For no device, HeLa cells not expressing NiCMM/iCMM were treated with either DMSO or 40 mM FCCP for 2 h. After the treatment, mitochondrial ROS was measured by MitoSOX. Box plot, center lines show the medians; box limits indicate the 25th and 75th percentiles as determined by R software; whiskers extend 1.5 times the interquartile range from the 25th and 75th percentiles, outliers are represented by dots. n = number of cells analyzed, from two independent experiments. p = Welch's t test. N.S., statistically non-significant.

not significant (Figures 5D and S6G). These results imply that mActZ-FY-induced morphological changes in mitochondria perturb both mitochondrial oxidative phosphorylation and glycolysis, as shown by measurement of the OCR and ECAR.

As ATP production in proliferating cells is attributed to glycolysis (Sun et al., 2019), we expected that the prolonged disruption of mitochondrial morphology by mActZ-FY would decrease intracellular ATP levels. However, similar to those in other stable cell lines, the overall ATP level and sensitivity to 2-deoxyglucose, a glycolysis inhibitor, in iCMM^{mActZ} cells remained unchanged with or without device actuation (Figures 5E–5H). Thus, alteration of mitochondrial morphology by mActZ-FY led to a decrease in OCR and ECAR but not a detectable change in intracellular ATP levels in the cells.

Together, these results indicate that the FiCEs should be suitably selected depending on the mitochondrial morphology and OCR/ECAR status to be induced.

iCMM-induced mitochondrial morphological changes do not render HeLa cells susceptible to staurosporine-induced apoptosis

The advantage of iCMM, a synthetic protein device, is that it does not directly modulate genes involved in mitochondrial dynamics, allowing us to examine the biological significance of mitochondrial morphology from unconventional perspectives. Therefore, we utilized iCMM to examine the effect of artificially constructed mitochondrial morphology on apoptosis.

During apoptosis, large intracellular structures reorganize to prepare for cell death (Elmore, 2007). One hallmark of this reorganization is mitochondrial fragmentation caused by an imbalance in the mitochondrial fusion-fission cycle (Karbowski and Youle, 2003; Wang and Youle, 2009). Using cells stably expressing iCMM, we found that the artificial disruption of mitochondrial morphology by iCMM did not commit cells to apoptosis, as shown by cleaved caspase-3 levels (Figure 6A, lane 1 and 2) and nuclear morphology (Figure 6B, upper graph). These results suggest that changes in mitochondrial morphology per se do not trigger intrinsic apoptosis.

We next examined whether iCMM-induced mitochondrial morphology changes would affect susceptibility to apoptosis induction. In this experiment, we set the concentration of staurosporine (STS), a potent apoptosis inducer, to induce apoptosis in less than 40% of DMSO-treated iCMM/NiCMM cells to examine whether iCMM-induced mitochondrial morphological changes promote apoptosis. Although the use of a previous, conventional genetic approach (modification of genes involved in mitochondrial dynamics) revealed that mitochondrial

Figure 3. iCMM alters mitochondrial morphology without loss of MMP

(A–D) MMP in HeLa cells expressing Tom20-CR and the indicated effector at each indicated time point after device actuation (50 nM rapamycin addition). Tom20-CR, slate blue; effector, yellow; TMRE, coral. Representative images at each time point are shown. Quantification was performed on three independent experiments. All data are presented as mean ± standard deviation. Cells expressing Tom20-CR and either mYF (0 min, n = 65; 30 min, n = 53; 120 min, n = 53), YF (0 min, n = 76; 30 min, n = 75; 120 min, n = 92), YF-Cav1s (0 min, n = 66; 30 min, n = 63; 120 min, n = 58), or mActZ-FY (0 min, n = 56; 30 min, n = 80; 120 min, n = 86) were analyzed. N.S., statistically non-significant compared with 0 min (Student's t test). Scale bar, 10 μm. LUTs (effector): 90–1,500, mYF (A), YF (B), and YF-Cav1s (C); 90–500, mActZ-FY (D).

(E–H) Time-lapse imaging (5 min/frame) of MMP in HeLa cells expressing Tom20-CR and the indicated effector. Before time-lapse imaging, the cells were treated with 50 nM rapamycin for 2 h. FCCP was added after image acquisition at frame 1. Quantification was performed on three independent experiments. All data are presented as mean ± standard deviation. Cells expressing Tom20-CR and either mYF (n = 90), YF (n = 84), YF-Cav1s (n = 59), or mActZ-FY (n = 67) were analyzed.

(I) (Left) Time course of the experiment performed in Figures 3E–3H. (Middle and right) Quantification was performed by using the results in Figures 3E–3H. Quantification was performed on three independent experiments. All data are presented as mean ± standard deviation. N.S., statistically non-significant (versus mYF, Student's t test).

CellPress
OPEN ACCESS

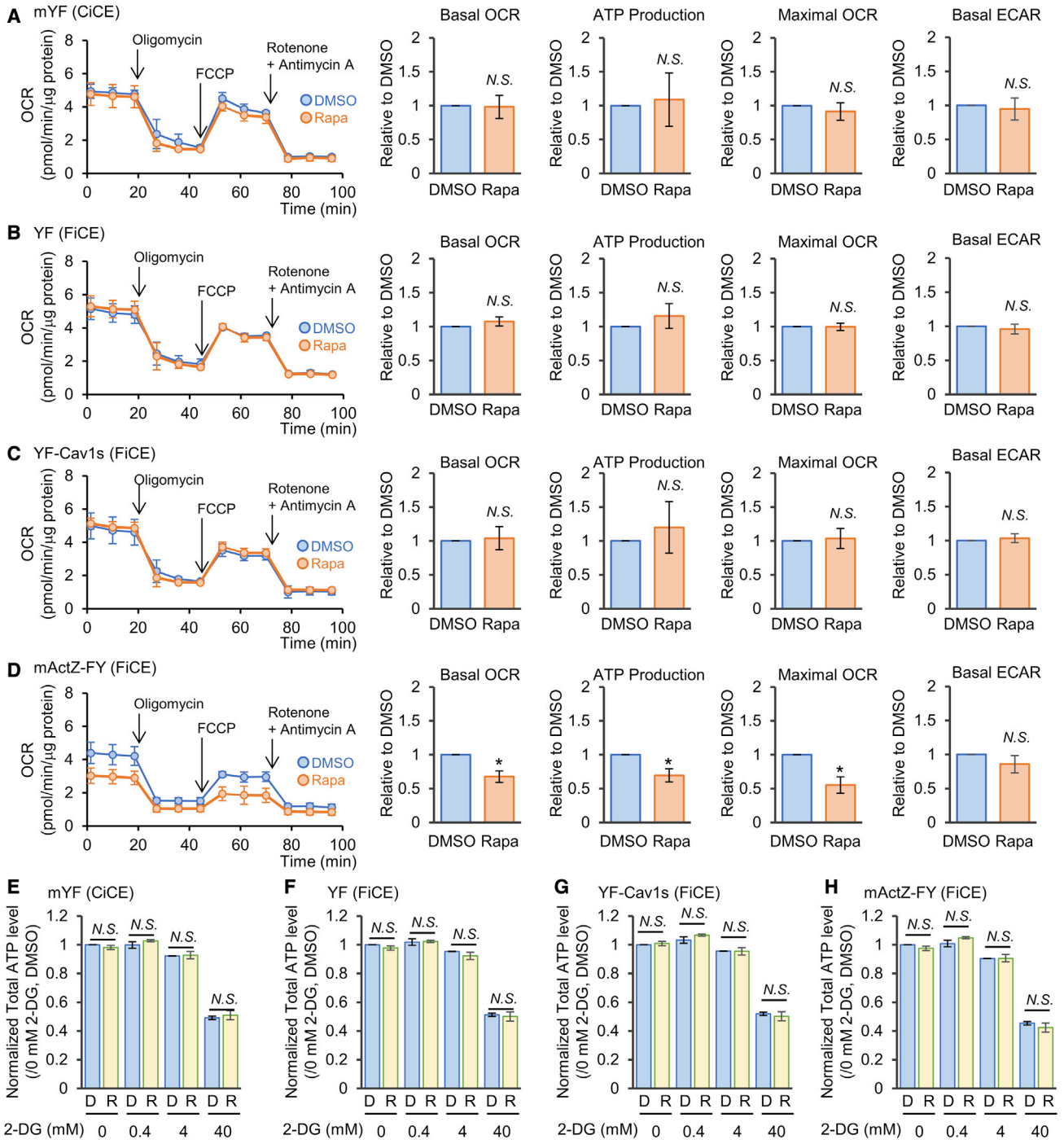

Figure 5. mActZ-FY-induced disruption of mitochondrial morphology affects OCR and ECAR

(A–D) OCR and ECAR in NiCMM (A), iCMM^{YF} (B), iCMM^{Cav1s} (C), and iCMM^{mActZ} cells (D). Before measurement, all cell lines were treated with DMSO or 50 nM rapamycin for 30 min. Quantification was performed on three independent experiments. All data are presented as mean ± standard deviation. *$p < 0.05$, N.S., statistically non-significant (paired t test).

(E–H) Intracellular ATP levels in NiCMM (E), iCMM^{YF} (F), iCMM^{Cav1s} (G), and iCMM^{mActZ} cells (H). Each cell line was treated with DMSO (D) or 50 nM rapamycin (R) for 1 h, followed by 2-DG treatment for 4 h. Quantification was performed on three independent experiments. All data are presented as mean ± standard deviation. N.S., statistically non-significant (Student's t test). See also Figure S6.

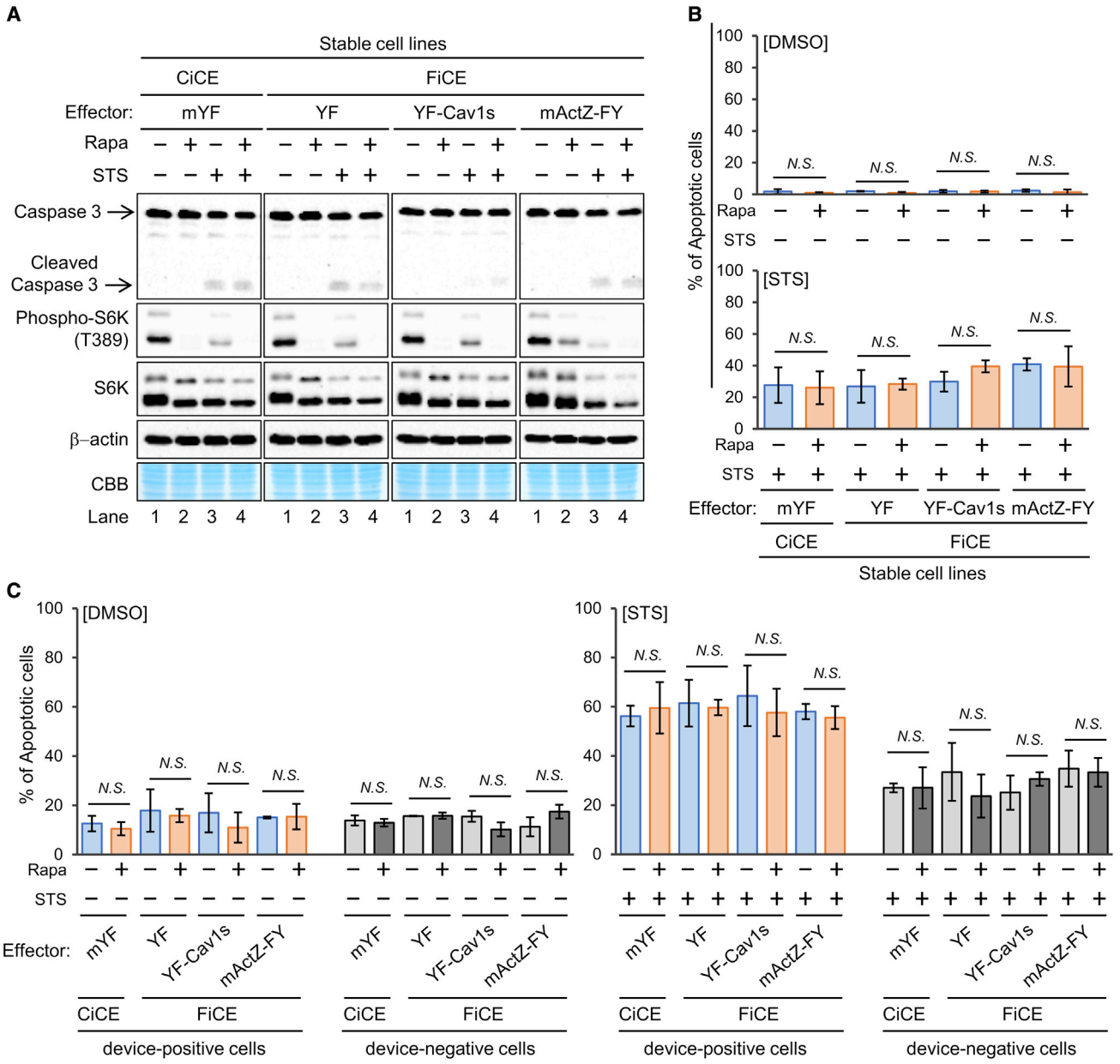

Figure 6. iCMM-induced changes in mitochondrial morphology do not affect STS-induced apoptosis

(A) HeLa cells stably expressing Tom20-CR and the indicated effector were treated with DMSO (Rapa [(−]) or 50 nM rapamycin (Rapa [+]) for 1 h, followed by treatment with 266 nM STS for 6 h. The cells were then subjected to western blotting.

(B) HeLa cells stably expressing Tom20-CR and the indicated effector were treated as in (A), and normal and apoptotic nuclei in the cells were counted. Quantification was performed on three independent experiments. All data are presented as mean ± standard deviation. Cells stably expressing Tom20-CR and either mYF (Rapa/STS = −/− (RS00): n = 539. Rapa/STS = +/− (RS10): n = 655. Rapa/STS = −/+ (RS01): n = 775. Rapa/STS = +/+ (RS11): n = 974), YF (RS00, n = 673; RS10, n = 643; RS01, n = 727; RS11, n = 695), YF-Cav1s (RS00, n = 1,182; RS10, n = 1,095; RS01, n = 864; RS11, n = 684), or mActZ-FY (RS00, n = 634; RS10, n = 630; RS01, n = 545; RS11, n = 568) were analyzed. N.S., statistically non-significant (Student's t test).

(C) HeLa cells transiently expressing Tom20-CR and the indicated effector were treated as in (A), and normal and apoptotic nuclei in cells expressing NiCMM/iCMM (device-positive cells) or not expressing NiCMM/iCMM (device-negative cells) were counted. Quantification was performed on three independent experiments. All data are presented as mean ± standard deviation. Cells transiently expressing Tom20-CR and either mYF (RS00, n = 242; RS10, n = 175; RS01, n = 223; RS11, n = 211), YF (RS00, n = 164; RS10, n = 202; RS01, n = 222; RS11, n = 198), YF-Cav1s (RS00, n = 101; RS10, n = 108; RS01, n = 194; RS11, n = 261) or mActZ-FY (RS00, n = 113; RS10, n = 131; RS01, n = 190; RS11, n = 208) and cells that did not express the device in the vicinity of cells expressing Tom20-CR and either mYF (RS00, n = 393; RS10, n = 292; RS01, n = 1,002; RS11, n = 554), YF (RS00, n = 294; RS10, n = 203; RS01, n = 794; RS11, n = 735), YF-Cav1s (RS00, n = 198; RS10, n = 209; RS01, n = 967; RS11, n = 995), or mActZ-FY (RS00, n = 246; RS10, n = 229; RS01, n = 851; RS11, n = 810) were analyzed. N.S., statistically non-significant (Student's t test). See also Figure S7.

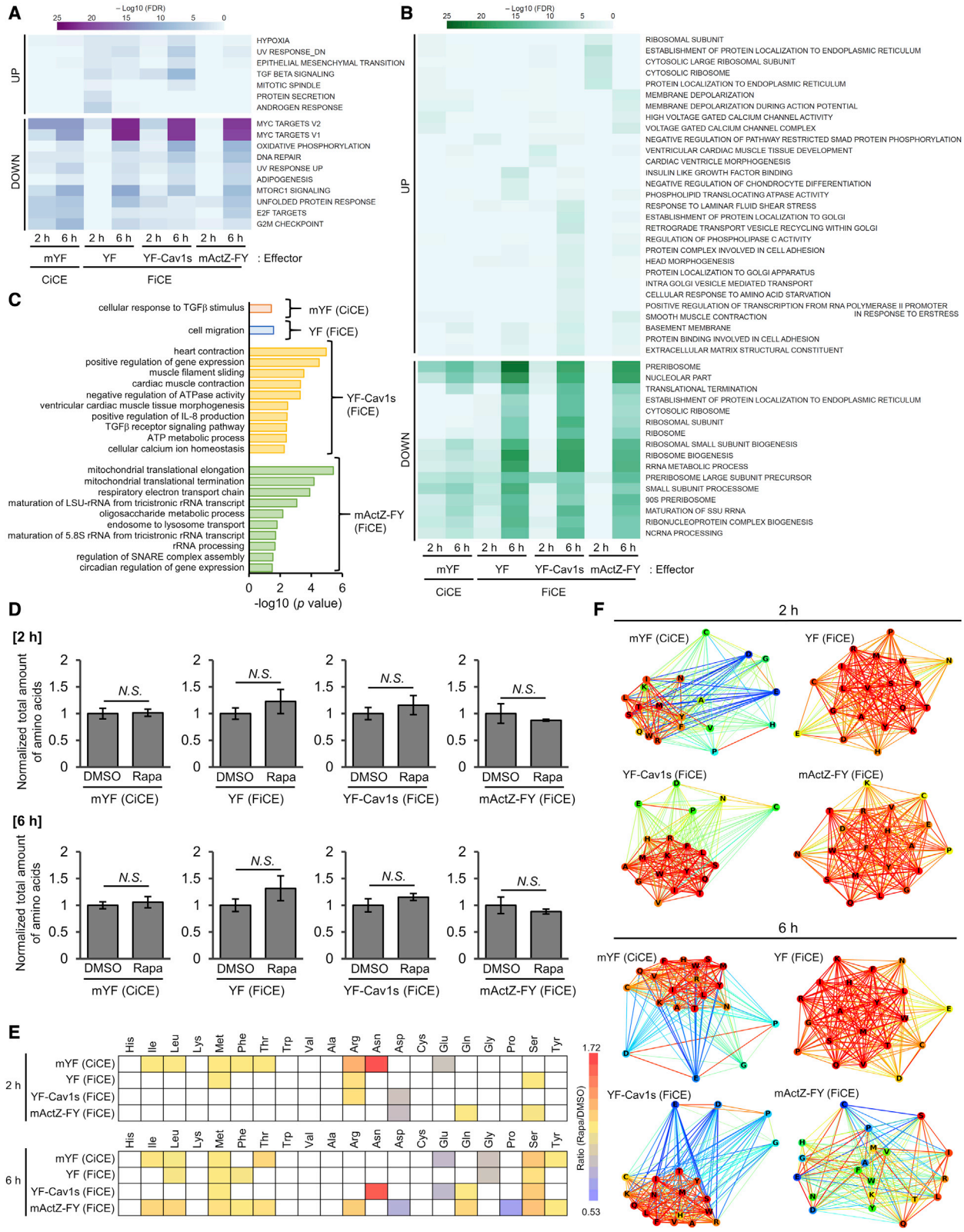

(legend on next page)

fragmentation could increase susceptibility to apoptosis-inducible input (Lee et al., 2004; Sugioka et al., 2004), we found that disruption of mitochondrial morphology by iCMM did not promote STS-induced apoptosis compared with cells stably expressing NiCMM, as shown by cleaved caspase-3 levels (Figure 6A, lane 3,4) and nuclear morphology (Figure 6B, lower graph). Similarly, when cells transiently expressing iCMM and NiCMM were compared, iCMM-induced mitochondrial morphological changes did not enhance STS-induced apoptosis (Figure 6C). Of note, cells transiently expressing iCMM/NiCMM were more susceptible to STS than the surrounding cells that did not express iCMM/NiCMM (Figure 6C), possibly because of damage caused by transient gene expression.

Intriguingly, we found that rapamycin, an allosteric mTORC1 inhibitor, failed to completely attenuate mTORC1 activity in iCMM^{mActZ} cells compared with other cell lines, as shown by the phosphorylation level of the mTORC1 substrate p70 S6 kinase (S6K) and the downward mobility shift of non-phosphorylated S6K (Figure 6A). However, STS-induced suppression of mTORC1 activity (Tee and Proud, 2001) in iCMM^{mActZ} cells was similar to that in other cells (Figure 6A). In addition, Torin 1, an ATP-competitive mTOR inhibitor, also completely suppressed mTORC1 activity in all cell types examined (Figure S7). These results suggest that rapamycin's inhibitory effect through its binding of FKBP12 and mTORC1 can be slightly suppressed by iCMM harboring mActZ-FY.

Rapid mitochondrial morphology changes induced by iCMM alter the transcriptome

An attractive aspect of synthetic biology is that it allows us to manipulate cellular behaviors by using rationally designed synthetic biomolecular devices. Although considerable efforts have been made to understand how biomolecules derived from inherent biological or artificially designed systems can be applied to devices, the applicability of organelle morphology to these synthetic biomolecular devices has not been explored because of technical limitations. To expand the possible range of applications of these devices, we examined how iCMM-induced changes in mitochondrial morphology modify gene expression in cells.

Gene set enrichment analysis (GSEA) of 50 "hallmark" gene sets representing major biological processes (Liberzon et al., 2015; Subramanian et al., 2005) revealed that changes in mitochondrial morphology induced by FiCE promoted the downregulation of MYC target expression irrespective of the mitochondrial morphology induced (Figure 7A). Gene ontology (GO) analysis demonstrated that iCMM-induced changes in mitochondrial morphology led to changes in various cellular functions, most notably decreased ribosomal functions (Figure 7B). Furthermore, GSEA and GO analysis did not report apoptosis as an iCMM-mediated cellular function (Figures 7A and 7B), supporting the notion that iCMM-induced changes in mitochondrial morphology per se did not affect apoptosis (Figure 6).

To further examine the effect of iCMM-induced changes in mitochondrial morphology on the transcriptome, we identified differentially expressed genes (DEGs) whose expression levels were significantly changed (defined as a fold change >2 and false discovery rate [FDR]-adjusted $p < 0.05$) (Figure S8 and Table S1). DEGs analysis revealed that the translocation of FiCE and CiCE to mitochondria per se did not affect the expression of genes involved in the mitochondrial fusion-fission cycle, as shown by the measurement of *DRP1*, *FIS1*, *RAB32*, *OPA1*, and *MFN1/2* (Table S1). Consistent with a previous report (Minster et al., 2016), *CREBRF* was identified as a DEG in rapamycin-treated cell lines expressing iCMM and NiCMM, highlighting the fidelity of the analysis (Table S1).

Among DEGs, 18, 31, 68, and 111 effector-specific DEGs were extracted from the use of mYF, YF, YF-Cav1s, and mActZ-FY, respectively (Table S1). GO analysis of the effector-specific DEGs demonstrated that the actuation of iCMM triggered diverse cellular functions depending on which effector was employed (Figure 7C). Notably, YF-Cav1s tended to increase the expression of genes related to actin-myosin interactions, whereas mActZ-FY appeared to decrease the expression of genes involved in mitochondrial translation (Figure 7C). These results suggest that the actuation of iCMM or NiCMM in target cells can provoke alteration of gene expression in an effector-dependent manner.

Rapid changes in mitochondrial morphology induced by iCMM alter the amino acid profile

All 20 amino acids, except for histidine, alanine, and cysteine, require mitochondrial enzymes for their metabolism (Guda et al., 2007). We thus hypothesized that iCMM-induced disruption of mitochondrial morphology would alter the intracellular amino acid profile. Although amino acids are well recognized

Figure 7. iCMM-induced mitochondrial morphology changes result in reorganization of the cellular transcriptome and amino acid profiles

Cells stably expressing Tom20-CR and the indicated effector were treated with either DMSO or 50 nM rapamycin for the indicated time and subsequently subjected to transcriptome analysis and amino acid profile analysis.

(A and B) Hallmark gene sets (A) and GO terms (B) enriched upon mitochondrial morphology changes in cells stably expressing Tom20-CR and the indicated effector were analyzed to yield heatmaps of $-\log_{10}$(FDR). FDR values were calculated by comparing DMSO- and rapamycin-treated cells for each effector at the indicated time points. Up/down indicates the direction of a transcriptomic change in rapamycin-treated cells compared with DMSO-treated cells. A maximum of 30 gene sets with FDR <0.01 in each direction and category are shown.

(C) Top 10 GO terms ($p < 0.05$) enriched in the effector-specific DEGs.

(D) Total amount of amino acids in cells stably expressing Tom20-CR and the indicated effector were analyzed after adding either DMSO or 50 nM rapamycin at the indicated time. Quantification was performed on three independent experiments. All data are presented as mean ± standard deviation. N.S., statistically non-significant (Student's t test).

(E) Amino acids with significantly altered proportions (criteria: $p < 0.05$, more than 10% change). White: amino acids that do not meet this criterion.

(F) Network graphs based on the correlation coefficient calculated for each amino acid. The color of each node represents the correlation with each amino acid based on serine, whereas the color of each edge represents the correlation between amino acids. Blue, low correlation coefficient; red, high correlation. The thickness of the edge represents the absolute value of the correlation coefficient. See also Figure S8.

as cues that modulate various signaling pathways, recent mathematical analysis has revealed that the comprehensive amino acid profile, not a single amino acid, plays a pivotal role in modulating cellular functions (Nishi et al., 2018). Therefore, we focused on the effect of iCMM on the proportion of individual amino acids among total amino acids. Although the total amount of amino acids did not differ significantly (Figure 7D), the proportion of various individual amino acids to the total amino acids was significantly altered in a FiCE-dependent manner after iCMM was turned on (Figure 7E). Interestingly, the reorganization of amino acid profiles was also observed in NiCMM cells (Figure 7E). However, histidine, alanine, cysteine, tryptophan, lysine, and valine are not associated with mitochondria, and did not show differential levels when any effector was activated (Figure 7E). These results suggest that the changes in amino acid profiles were caused at least partially by effector accumulation in mitochondria.

All amino acid metabolism is coordinately regulated in the cell to create an appropriate amino acid profile in accordance with the circumstances. To further analyze the interplay between iCMM and amino acids, we examined correlations among amino acids. Network architectures reflecting amino acid correlations were similar in NiCMM and iCMM^{Cav1s} cells and in iCMM^{YF} and iCMM^{mActZ} cells (Figure 7F). In NiCMM and iCMM^{Cav1s} cells, glutamate, aspartate, and proline, which are regulated by p53-mediated amino acid metabolism in the vicinity of mitochondria, presented a low correlation with serine that is critical for mitochondrial dynamics and functions (Gao et al., 2018) (Figure 7F). However, in iCMM^{YF} cells, nearly all amino acids presented a strong correlation with serine, whereas correlations among amino acids in iCMM^{mActZ} cells disappeared over time (Figure 7F). These results suggest that iCMM and NiCMM actuation led to alteration of the coordination of amino acid metabolism.

DISCUSSION

Recent advances in life sciences have transformed cells into objects of not only understanding but also manipulation. A comprehensive understanding of intrinsic biological systems through reductionistic approaches (e.g., molecular biology) is necessary to develop techniques for manipulating cells. On the other hand, the manipulation of cells by using constructive approaches (e.g., synthetic biology) can facilitate the understanding of biological systems. The harmonization of insights obtained from reductionistic and constructive approaches provides a valuable opportunity to synergistically advance both our understanding of the cell and the development of manipulation strategies.

In this study, we developed three FiCEs capable of inducing different mitochondrial morphologies on a minute timescale and investigated the effect of iCMM on intracellular biological systems. In general, the biological significance of mitochondrial morphology in physiopathology has been reported from the analysis of phenotypes obtained by altering the expression of proteins involved in mitochondrial dynamics. However, the application of iCMM, which can induce mitochondrial morphological changes orthogonal to the conventional genetic approaches, will not only highlight this significance from a new perspective but also lead to the development of new technologies to control cellular functions by regulating mitochondrial morphology. For example, as intracellular mitochondrial distribution is determined by mitochondrial demand at the subcellular compartment level (Westermann, 2012), iCMM could perturb this demand by disrupting the mitochondrial distribution in the cell, which would otherwise be challenging. Besides, given the growing interest in organelle morphology over the decades, synthetic biology-based approaches such as iCMM could serve as powerful platforms for unraveling the significance of the morphologies of various organelles in biological systems.

Here, we utilized a rapamycin-based CID system to develop the iCMM. If inhibition of mTORC1 by rapamycin affects the interpretation of the experimental results, other CID systems (such as abscisic acid, gibberellin, synthetic ligand of FKBP'-trimethoprim-induced dimerization system) (Liang et al., 2011; Liu et al., 2014; Miyamoto et al., 2012) or optogenetic techniques should be selected depending on the purpose of the experiment. In such cases, the optimization (e.g., fluorescent protein selection, an arrangement of functional domains, etc.) of effectors and the anchor is necessary. Although we developed four effectors (one CiCE and three FiCEs) and one mitochondria-specific anchor in the present study, we recognize that they could be further refined according to their purpose. For example, if the dimeric YFP used for FiCE with Cav1s or mActZ is problematic, it is possible to use monomeric fluorescent proteins (such as mCherry) instead (Figure S9).

Previous studies have reported that enhanced mitochondrial fragmentation results in the disorganization of cristae remodeling, leading to a decrease in OCR and a complementary increase in ECAR (Buck et al., 2016; Khacho et al., 2014). In contrast, we found that mitochondrial fragmentation by mActZ-FY, but not other effectors, significantly reduced both OCR and ECAR. One possible reason for this decrease in OCR and ECAR is that reorganization of the actin skeleton architecture by mActZ-FY around mitochondria might have a suppressive effect on oxidative phosphorylation and the glycolytic system. In fact, actin skeleton architecture has been reported to be involved in regulating oxidative phosphorylation and the glycolytic system (Casalena et al., 2016; Park et al., 2020). Although further research (e.g., reconstruction of the mActZ-FY-induced actin skeletal architecture around the mitochondria without inducing mitochondrial morphological changes) is needed to understand the detailed mechanisms, we believe that mActZ-FY could be useful in elucidating the relationship between actin skeleton architecture and the metabolic phenotype defined by OCR and ECAR. Furthermore, our results suggest that mActZ-FY is a useful FiCE for manipulating OCR and ECAR at any given time point.

Mitochondrial fragmentation is a major hallmark of apoptosis, but why mammalian cells have internalized the process of apoptosis during evolution and the biological significance of this internalization remains controversial. We expected iCMM-induced changes in mitochondrial morphology to alter the sensitivity of mitochondria to apoptosis inducers, but, contrary to our expectations, iCMM did not alter the sensitivity of HeLa cells to STS, at least under our experimental conditions. These results suggest that the process that leads to a certain mitochondrial morphology, rather than the morphology per se, might be more critical in determining sensitivity to

apoptosis inducers. For example, overexpression of the human cytomegalovirus-encoded protein viral mitochondria-localized inhibitor of apoptosis (vMIA) causes mitochondrial fragmentation. However, vMIA also exhibits anti-apoptotic effects as it binds and inhibits proapoptotic Bcl-2 family members (Norris and Youle, 2008). Future studies using various cell lines and apoptosis inducers will provide a comprehensive understanding of the relationship between mitochondrial morphology and apoptosis. We are confident that iCMM will prove to be a valuable tool in these studies with the development of appropriate effectors.

Notably, we found that the effect of rapamycin on mTORC1 was slightly attenuated in cells stably expressing mActZ-FY and Tom20-CR. Because the activity of mTORC1 was completely suppressed by rapamycin in other cells stably expressing iCMM/NiCMM, exogenously expressed FKBP and FRB are unlikely to be the main cause of the inhibitory effect of rapamycin on mTORC1 activity in iCMM^{mActZ} cells. Although it is well appreciated that mTORC1 mainly localizes to lysosomes, several reports indicate that mTORC1 also localizes to mitochondria (Betz and Hall, 2013). Meanwhile, although the localization of endogenous FKBP12 has not been clarified, the results from tagging with fluorescent proteins (mYF and YF in this study) indicate that it is diffusely localized throughout the cell. Therefore, even if changes in mitochondrial morphology induced by mActZ-FY alter the localization of mTORC1, this change does not appear to affect rapamycin-mediated suppression of mTORC1 via FKBP12. However, it is conceivable that reorganization of the actin skeleton architecture around mitochondria might have interfered with the rapamycin-regulated binding of mTORC1 and FKBP12. Given that rapamycin and its derivatives are promising therapeutics for cancers, further studies to elucidate the mechanism by which mActZ-FY attenuates the effects of rapamycin on mTORC1 activity would be useful for both basic and clinical research. In addition, the development of strategies to completely inhibit the effects of rapamycin on endogenous mTORC1 activity in a target cell will lead to the development of more complex and sophisticated rapamycin-based synthetic biomolecular devices.

Mitochondria transfer their genetic information to the host cell nucleus in the course of an endosymbiotic relationship. Therefore, retrograde signaling, a communication system from mitochondria to the nucleus, is a prerequisite to coordinate mitochondrial functions with the nucleic transcription machinery under various physiopathological conditions. In this study, we found that the induction of mitochondrial morphological changes by iCMM reduced the expression of MYC targets and ribosomal-related genes. There is no reliable evidence to mechanistically explain why the changes in mitochondrial morphology led to the impairment of MYC target and ribosome-related gene expression. However, a potential molecule to bridge this gap is MYC. The MYC family, an oncogene family, dysregulated in >50% of human cancers, regulates the transcription of at least 15% of the entire genome (Dang et al., 2006), indicating the multifunctionality of MYC in biological systems. Remarkably, MYC plays a pivotal role in regulating ribosome biogenesis (Van Riggelen et al., 2010). In addition, over several decades, many studies have suggested an intimate relationship between MYC and mitochondria (Morrish and Hockenbery, 2014; Zhang et al., 2017). Our results also provide additional support for the relationship between MYC and mitochondria. Although the molecular puzzle underlying the MYC-mitochondria-ribosome axis remains unsolved, the finding that iCMM-induced changes in mitochondrial morphology reduced the expression of MYC- and ribosome-related genes provides one part of the solution.

We also found that the FiCEs and CiCE developed in this study induced characteristic gene expression and amino acid profiles. These results show that perturbations in mitochondria (not only morphological changes but also the accumulation of extrinsic effector proteins in mitochondria) could alter cellular gene expression and amino acid profiles. Further studies, including comparisons with conventional methods, will provide detailed mechanistic insights into the mitochondrial signaling evoked by changes in mitochondrial morphology and resulting changes in the transcriptome and amino acid profile.

In summary, the iCMM system developed in this study allows the effective and rapid manipulation of mitochondrial morphology. In combination with conventional genetic approaches, iCMM m provide new insights into the physiopathological functions of mitochondrial morphology in health and disease. In this study, we mainly used HeLa cells (human cervical adenocarcinoma) for our experiments, but further comprehensive studies using other cancer cell lines and normal cells are required to understand the effects of iCMM-induced mitochondrial morphological changes on cells. We envision that one promising application of iCMM might involve the treatment of a variety of diseases. If we could alter the properties of cells (e.g., omics information) by inducing mitochondrial morphological changes at appropriate time points, this would lead to the development of new therapeutic strategies for diseases. It is also possible to study how the phenotype changes by disrupting giant mitochondria observed in various pathological tissues (such as the liver, heart, and nerve tissue) with iCMM. In life science research, the high spatial and temporal resolution of iCMM might be applied to the manipulation of local communication between the mitochondria and other organelles. Although we have a long way to go to grasp the biological significance of the ever-changing mitochondrial morphology in a cell, there is no doubt that mitochondrial morphology is more than just a phenotype.

Limitations of study

Although iCMM can artificially change the morphology of the mitochondria without losing MMP, transferring extrinsic genes and addition of chemical dimerizer (or laser irradiation) into the target cells are necessary to activate iCMM. Therefore, when comparing the effects of the change in artificial mitochondrial morphology by iCMM with the effects of the change in conventional physiological mitochondrial morphology (e.g., downregulation of DRP1 or OPA1), it is necessary to interpret the results by considering the characteristics of both methods. For example, Li et al. (2020) reported that knockdown of OPA1 in Huh7 cells altered the expression of metabolism-related genes. However, no such changes were observed when mitochondrial morphological changes were induced by iCMM in HeLa cells (Figure 7). Although differences in cell

type might be one reason, we recognize that the mitochondrial morphological changes caused by iCMM that have developed in this study do not produce exactly the same results as physiological mitochondrial morphological changes. The development of iCMM that can induce changes in intracellular information similar to those induced by physiological mitochondrial morphological changes is an important obstacle to be overcome in the future. However, it should be noted that when physiological mitochondrial morphology change is achieved by regulating gene expression, the expression levels of genes other than the target gene might also change in conjunction. Moreover, changes in mitochondrial morphology in various pathological conditions are thought to be the result of incredibly complicated changes in intracellular information. Accordingly, it might be challenging to obtain the same output caused by physiological mitochondrial morphological changes with iCMM alone. Although the term mitochondrial morphology is simple, it should be considered that it encompasses a wide variety of biological information, including the spatiotemporal distribution and heterogeneous activity of mitochondria and their crosstalk with other organelles. We believe that it is useful to integrate conventional genetic methods with artificial morphological manipulation methods such as iCMM in order to solve the fundamental question of why the mitochondria show different morphologies depending on the conditions.

STAR★METHODS

Detailed methods are provided in the online version of this paper and include the following:

- KEY RESOURCES TABLE
- RESOURCE AVAILABILITY
  - Lead contact
  - Materials availability
  - Data and code availability
- EXPERIMENTAL MODEL AND SUBJECT DETAILS
  - Cell culture and media
- METHOD DETAILS
  - Plasmid construction
  - Transient transfection
  - Real-time reverse-transcription polymerase chain reaction
  - Lentivirus production
  - Establishment of HeLa cells stably expressing the iCMM system
  - Live-cell imaging
  - CLEM
  - Immunocytochemistry
  - Mitochondrial ROS measurement
  - Mitochondrial membrane potential analysis
  - Extracellular flux analysis
  - ATP measurement
  - Cell proliferation assay
  - RNA-seq
  - Amino acid profile analysis
  - Apoptosis analysis
  - Western blot analysis
- QUANTIFICATION AND STATISTICAL ANALYSIS
  - Mitochondrial morphology analysis
  - Transcriptome analysis
  - Amino acid correlation network analysis
  - Statistical analysis

SUPPLEMENTAL INFORMATION

Supplemental information can be found online at https://doi.org/10.1016/j.crmeth.2021.100052.

ACKNOWLEDGMENTS

We thank Katsuyuki Suzuki, Akira Takebe (JEOL Ltd), and Katsuko Okubo (University of Tsukuba) for technical assistance; Keita Takahashi (NikonInstech Co., Ltd); Hiroyuki Soejima (Tokyo Science Co., Ltd.); and Yasuko Maruyama (University of Tsukuba) for generous support. We would like to thank Editage (www.editage.com) for English language editing. This study was supported in part by grant-in-aid for Scientific Research on Innovative Areas (18H04854), Leading Initiative for Excellent Young Researchers, JST CREST (JPMJCR1927), and JST COI-NEXT (JPMJPF2017).

AUTHOR CONTRIBUTIONS

T. Miyamoto conceived the project. T. Miyamoto designed the experiments. T. Miyamoto, H.U., Y.M., S.I.H., S.G., D.Y., M.M., Y.Y., H.N., N.H., Y.T., M.S., T. Matsuzaka, F.H., H.O., SI.T., N.Y., K.I., and H.S. conducted the experiments. T. Miyamoto and H.U. wrote the article.

DECLARATION OF INTERESTS

The authors declare no competing interests.

Received: December 3, 2020
Revised: March 12, 2021
Accepted: June 22, 2021
Published: July 22, 2021

REFERENCES

Archer, S.L. (2013). Mitochondrial dynamics–mitochondrial fission and fusion in human diseases. N. Engl. J. Med. *369*, 2236–2251.

Betz, C., and Hall, M.N. (2013). Where is mTOR and what is it doing there? J. Cell Biol. *203*, 563–574.

Buck, M.D.D., O'Sullivan, D., Klein Geltink, R.I.I., Curtis, J.D.D., Chang, C.H., Sanin, D.E.E., Qiu, J., Kretz, O., Braas, D., van der Windt, G.J.J.W., et al. (2016). Mitochondrial dynamics controls T cell fate through metabolic programming. Cell *166*, 63–76.

Casalena, G., Bottinger, E., and Daehn, I. (2016). TGFβ-induced actin cytoskeleton rearrangement in podocytes is associated with compensatory adaptation of mitochondrial energy metabolism. Nephron *131*, 278–284.

Cassidy-Stone, A., Chipuk, J.E., Ingerman, E., Song, C., Yoo, C., Kuwana, T., Kurth, M.J., Shaw, J.T., Hinshaw, J.E., Green, D.R., et al. (2008). Chemical inhibition of the mitochondrial division dynamin reveals its role in Bax/Bak-dependent mitochondrial outer membrane permeabilization. Dev. Cell *14*, 193–204.

Chen, H., Chomyn, A., and Chan, D.C. (2005). Disruption of fusion results in mitochondrial heterogeneity and dysfunction. J. Biol. Chem. *280*, 26185–26192.

Clarke, L., and Kitney, R. (2020). Developing synthetic biology for industrial biotechnology applications. Biochem. Soc. Trans. *48*, 113–122.

Csordás, G., Várnai, P., Golenár, T., Roy, S., Purkins, G., Schneider, T.G., Balla, T., and Hajnóczky, G. (2010). Imaging interorganelle contacts and local calcium dynamics at the ER-mitochondrial interface. Mol. Cell *39*, 121–132.

Dang, C.V., O'Donnell, K.A., Zeller, K.I., Nguyen, T., Osthus, R.C., and Li, F. (2006). The c-Myc target gene network. Semin. Cancer Biol. *16*, 253–264.

Derose, R., Miyamoto, T., and Inoue, T. (2013). Manipulating signaling at will: chemically-inducible dimerization (CID) techniques resolve problems in cell biology. Pflugers Arch. Eur. J. Physiol. *465*, 409–417.

Detmer, S.A., and Chan, D.C. (2007). Functions and dysfunctions of mitochondrial dynamics. Nat. Rev. Mol. Cell Biol. *8*, 870–879.

Dobin, A., Davis, C.A., Schlesinger, F., Drenkow, J., Zaleski, C., Jha, S., Batut, P., Chaisson, M., and Gingeras, T.R. (2013). STAR: ultrafast universal RNA-seq aligner. Bioinformatics *29*, 15–21.

Elmore, S. (2007). Apoptosis: a review of programmed cell death. Toxicol. Pathol. *35*, 495–516.

Fegan, A., White, B., Carlson, J.C.T., and Wagner, C.R. (2010). Chemically controlled protein assembly: techniques and applications. Chem. Rev. *110*, 3315–3336.

Folcher, M., and Fussenegger, M. (2012). Synthetic biology advancing clinical applications. Curr. Opin. Chem. Biol. *16*, 345–354.

Gao, X., Lee, K., Reid, M.A., Sanderson, S.M., Qiu, C., Li, S., Liu, J., and Locasale, J.W. (2018). Serine availability influences mitochondrial dynamics and function through lipid metabolism. Cell Rep. *22*, 3507–3520.

Golsteyn, R.M., Beckerle, M.C., Koay, T., and Friederich, E. (1997). Structural and functional similarities between the human cytoskeletal protein zyxin and the ActA protein of Listeria monocytogenes. J. Cell Sci. *110*, 1893–1906.

Gray, M.W., Burger, G., and Franz Lang, B. (2001). The origin and early evolution of mitochondria. Genome Biol. *2*, 1–5.

Grozinger, L., Amos, M., Gorochowski, T.E., Carbonell, P., Oyarzún, D.A., Stoof, R., Fellermann, H., Zuliani, P., Tas, H., and Goñi-Moreno, A. (2019). Pathways to cellular supremacy in biocomputing. Nat. Commun. *10*, 1–11.

Guda, P., Guda, C., and Subramaniam, S. (2007). Reconstruction of pathways associated with amino acid metabolism in human mitochondria. Genomics Proteomics Bioinformatics *5*, 166–176.

Hsieh, C.W., Chu, C.H., Lee, H.M., and Yuan Yang, W. (2015). Triggering mitophagy with far-red fluorescent photosensitizers. Sci. Rep. *5*, 1–12.

Ichinohe, T., Yamazaki, T., Koshiba, T., and Yanagi, Y. (2013). Mitochondrial protein mitofusin 2 is required for NLRP3 inflammasome activation after RNA virus infection. Proc. Natl. Acad. Sci. U S A *110*, 17963–17968.

Inoue, T., Heo, W. Do, Grimley, J.S., Wandless, T.J., and Meyer, T. (2005). An inducible translocation strategy to rapidly activate and inhibit small GTPase signaling pathways. Nat. Methods *2*, 415–418.

Jakobs, S., Martini, N., Schauss, A.C., Egner, A., Westermann, B., and Hell, S.W. (2003). Spatial and temporal dynamics of budding yeast mitochondria lacking the division component Fis1p. J. Cell Sci. *116*, 2005–2014.

Kakimoto, Y., Tashiro, S., Kojima, R., Morozumi, Y., Endo, T., and Tamura, Y. (2018). Visualizing multiple inter-organelle contact sites using the organelle-targeted split-GFP system. Sci. Rep. *8*, 1–13.

Karbowski, M., and Youle, R.J. (2003). Dynamics of mitochondrial morphology in healthy cells and during apoptosis. Cell Death Differ. *10*, 870–880.

Khacho, M., Tarabay, M., Patten, D., Khacho, P., MacLaurin, J.G., Guadagno, J., Bergeron, R., Cregan, S.P., Harper, M.E., Park, D.S., et al. (2014). Acidosis overrides oxygen deprivation to maintain mitochondrial function and cell survival. Nat. Commun. *5*, 1–15.

Khalil, A.S., and Collins, J.J. (2010). Synthetic biology: applications come of age. Nat. Rev. Genet. *11*, 367–379.

Koshiba, T., Yasukawa, K., Yanagi, Y., and Kawabata, S. (2011). Mitochondrial membrane potential is required for MAVS-mediated antiviral signaling. Sci. Signal. *4*, 1–8.

Lambert, T.J. (2019). FPbase: a community-editable fluorescent protein database. Nat. Methods *16*, 277–278.

Lee, Y., Jeong, S.-Y., Karbowski, M., Smith, C.L., and Youle, R.J. (2004). Roles of the mammalian mitochondrial fission and fusion mediators Fis1, Drp1, and Opa1 in apoptosis. Mol. Biol. Cell *15*, 5001–5011.

Leonard, A.P., Cameron, R.B., Speiser, J.L., Wolf, B.J., Peterson, Y.K., Schnellmann, R.G., Beeson, C.C., and Rohrer, B. (2015). Quantitative analysis of mitochondrial morphology and membrane potential in living cells using high-content imaging, machine learning, and morphological binning. Biochim. Biophys. Acta Mol. Cell Res. *1853*, 348–360.

Lerner, C., Bitto, A., Pulliam, D., Nacarelli, T., Konigsberg, M., Van Remmen, H., Torres, C., and Sell, C. (2013). Reduced mammalian target of rapamycin activity facilitates mitochondrial retrograde signaling and increases life span in normal human fibroblasts. Aging Cell *12*, 966–977.

Li, M., Wang, L., Wang, Y., Zhang, S., Zhou, G., Lieshout, R., Ma, B., Liu, J., Qu, C., Verstegen, M.M.A., et al. (2020). Mitochondrial fusion via OPA1 and MFN1 supports liver tumor cell metabolism and growth. Cells *9*, 1–16.

Liang, F.S., Ho, W.Q., and Crabtree, G.R. (2011). Engineering the ABA plant stress pathway for regulation of induced proximity. Sci. Signal. *4*, 1–10.

Liao, Y., Smyth, G.K., and Shi, W. (2014). FeatureCounts: an efficient general purpose program for assigning sequence reads to genomic features. Bioinformatics *30*, 923–930.

Liberzon, A., Subramanian, A., Pinchback, R., Thorvaldsdóttir, H., Tamayo, P., and Mesirov, J.P. (2011). Molecular signatures database (MSigDB) 3.0. Bioinformatics *27*, 1739–1740.

Liberzon, A., Birger, C., Thorvaldsdóttir, H., Ghandi, M., Mesirov, J.P., and Tamayo, P. (2015). The molecular signatures database hallmark gene set collection. Cell Syst. *1*, 417–425.

Liu, P., Calderon, A., Konstantinidis, G., Hou, J., Voss, S., Chen, X., Li, F., Banerjee, S., Hoffmann, J.E., Theiss, C., et al. (2014). A bioorthogonal small-molecule-switch system for controlling protein function in live cells. Angew. Chem. Int. Ed. *53*, 10049–10055.

Lomakin, A.J., Cattin, C.J., Cuvelier, D., Alraies, Z., Molina, M., Nader, G.P.F., Srivastava, N., Saez, P.J., Garcia-Arcos, J.M., Zhitnyak, I.Y., et al. (2020). The nucleus acts as a ruler tailoring cell responses to spatial constraints. Science *370*, eaba2894.

McCarthy, D.J., Chen, Y., and Smyth, G.K. (2012). Differential expression analysis of multifactor RNA-seq experiments with respect to biological variation. Nucleic Acids Res. *40*, 4288–4297.

Minster, R.L., Hawley, N.L., Su, C.T., Sun, G., Kershaw, E.E., Cheng, H., Buhule, O.D., Lin, J., Reupena, M.S., Viali, S., et al. (2016). A thrifty variant in CREBRF strongly influences body mass index in Samoans. Nat. Genet. *48*, 1049–1054.

Miyamoto, T., DeRose, R., Suarez, A., Ueno, T., Chen, M., Sun, T.P., Wolfgang, M.J., Mukherjee, C., Meyers, D.J., and Inoue, T. (2012). Rapid and orthogonal logic gating with a gibberellin-induced dimerization system. Nat. Chem. Biol. *8*, 465–470.

Miyamoto, T., Razavi, S., Derose, R., and Inoue, T. (2013). Synthesizing biomolecule-based boolean logic gates. ACS Synth. Biol. *2*, 72–82.

Miyamoto, T., Rho, E., Sample, V., Akano, H., Magari, M., Ueno, T., Gorshkov, K., Chen, M., Tokumitsu, H., Zhang, J., et al. (2015). Compartmentalized AMPK signaling illuminated by genetically encoded molecular sensors and actuators. Cell Rep. *11*, 657–670.

Morrish, F., and Hockenbery, D. (2014). MYC and mitochondrial biogenesis. Cold Spring Harb. Perspect. Med. *4*, a014225.

Nakamura, H., Rho, E., Deng, D., Razavi, S., Matsubayashi, H.T., and Inoue, T. (2020). ActuAtor, a molecular tool for generating force in living cells: controlled deformation of intracellular structures. BioRxiv, 2020.03.30.016360.

Nishi, H., Yamanaka, D., Kamei, H., Goda, Y., Kumano, M., Toyoshima, Y., Takenaka, A., Masuda, M., Nakabayashi, Y., Shioya, R., et al. (2018). Importance of serum amino acid profile for induction of hepatic steatosis under protein malnutrition. Sci. Rep. *8*, 1–11.

Norris, K.L., and Youle, R.J. (2008). Cytomegalovirus proteins vMIA and m38.5 link mitochondrial morphogenesis to Bcl-2 family proteins. J. Virol. *82*, 6232–6243.

Park, J.S., Burckhardt, C.J., Lazcano, R., Solis, L.M., Isogai, T., Li, L., Chen, C.S., Gao, B., Minna, J.D., Bachoo, R., et al. (2020). Mechanical regulation of glycolysis via cytoskeleton architecture. Nature *578*, 621–626.

Parton, R.G., and Simons, K. (2007). The multiple faces of caveolae. Nat. Rev. Mol. Cell Biol. *8*, 185–194.

Picard, M., Shirihai, O.S., Gentil, B.J., and Burelle, Y. (2013). Mitochondrial morphology transitions and functions: implications for retrograde signaling? Am. J. Physiol. Regul. Integr. Comp. Physiol. *304*, R393–R406.

Putyrski, M., and Schultz, C. (2012). Protein translocation as a tool: the current rapamycin story. FEBS Lett. *586*, 2097–2105.

R Core Team (2017). (2017). R: A Language and Environment for Statistical Computing. https://www.R-project.org/.

Rapaport, D., Brunner, M., Neupert, W., and Westermann, B. (1998). Fzo1p is a mitochondrial outer membrane protein essential for the biogenesis of functional mitochondria in *Saccharomyces cerevisiae*. J. Biol. Chem. *273*, 20150–20155.

Van Riggelen, J., Yetil, A., and Felsher, D.W. (2010). MYC as a regulator of ribosome biogenesis and protein synthesis. Nat. Rev. Cancer *10*, 301–309.

Robinson, M.D., McCarthy, D.J., and Smyth, G.K. (2009). edgeR: a Bioconductor package for differential expression analysis of digital gene expression data. Bioinformatics *26*, 139–140.

Rosario, F.J., Gupta, M.B., Myatt, L., Powell, T.L., Glenn, J.P., Cox, L., and Jansson, T. (2019). Mechanistic target of rapamycin complex 1 promotes the expression of genes encoding electron transport chain proteins and stimulates oxidative phosphorylation in primary human trophoblast cells by regulating mitochondrial biogenesis. Sci. Rep. *9*, 1–14.

Schindelin, J., Arganda-Carreras, I., Frise, E., Kaynig, V., Longair, M., Pietzsch, T., Preibisch, S., Rueden, C., Saalfeld, S., Schmid, B., et al. (2012). Fiji: an open-source platform for biological-image analysis. Nat. Methods *9*, 676–682.

Schlegel, A., and Lisanti, M.P. (2000). A molecular dissection of caveolin-1 membrane attachment and oligomerization. Two separate regions of the caveolin-1 c-terminal domain mediate membrane binding and oligomer/oligomer interactions in vivo. J. Biol. Chem. *275*, 21605–21617.

Smeitink, J.A., Zeviani, M., Turnbull, D.M., and Jacobs, H.T. (2006). Mitochondrial medicine: a metabolic perspective on the pathology of oxidative phosphorylation disorders. Cell Metab. *3*, 9–13.

Smith, G.A., and Portnoy, D.A. (1997). How the *Listeria monocytogenes* ActA protein converts actin polymerization into a motile force. Trends Microbiol. *5*, 272–276.

Subramanian, A., Tamayo, P., Mootha, V.K., Mukherjee, S., Ebert, B.L., Gillette, M.A., Paulovich, A., Pomeroy, S.L., Golub, T.R., Lander, E.S., et al. (2005). Gene set enrichment analysis: a knowledge-based approach for interpreting genome-wide expression profiles. Proc. Natl. Acad. Sci. U S A *102*, 15545–15550.

Sugioka, R., Shimizu, S., and Tsujimoto, Y. (2004). Fzo1, a protein involved in mitochondrial fusion, inhibits apoptosis. J. Biol. Chem. *279*, 52726–52734.

Sun, H., Chen, L., Cao, S., Liang, Y., and Xu, Y. (2019). Warburg effects in cancer and normal proliferating cells: two tales of the same name. Genomics Proteomics Bioinformatics *17*, 273–286.

Tao, Y., Yang, Y., Zhou, R., and Gong, T. (2020). Golgi apparatus: an emerging platform for innate immunity. Trends Cell Biol *30*, 467–477.

Tee, A.R., and Proud, C.G. (2001). Staurosporine inhibits phosphorylation of translational regulators linked to mTOR. Cell Death Differ. *8*, 841–849.

Twig, G., Hyde, B., and Shirihai, O.S. (2008). Mitochondrial fusion, fission and autophagy as a quality control axis: the bioenergetic view. Biochim. Biophys. Acta Bioenerg. *1777*, 1092–1097.

Venturini, V., Pezzano, F., Català Castro, F., Häkkinen, H.-M., Jiménez-Delgado, S., Colomer-Rosell, M., Marro, M., Tolosa-Ramon, Q., Paz-López, S., Valverde, M.A., et al. (2020). The nucleus measures shape changes for cellular proprioception to control dynamic cell behavior. Science *370*, eaba2644.

Wai, T., and Langer, T. (2016). Mitochondrial dynamics and metabolic regulation. Trends Endocrinol. Metab. *27*, 105–117.

Wang, C., and Youle, R.J. (2009). The role of mitochondria in apoptosis. Annu. Rev. Genet. *43*, 95–118.

Westermann, B. (2012). Bioenergetic role of mitochondrial fusion and fission. Biochim. Biophys. Acta Bioenerg. *1817*, 1833–1838.

Yang, J.Y., and Yang, W.Y. (2011). Spatiotemporally controlled initiation of Parkin-mediated mitophagy within single cells. Autophagy *7*, 1230–1238.

Yu-Wai-Man, P., and Chinnery, P.F. (2012). Dysfunctional mitochondrial maintenance: what breaks the circle of life? Brain *135*, 9–11.

Zhang, K., Li, H., and Song, Z. (2014). Membrane depolarization activates the mitochondrial protease OMA1 by stimulating self-cleavage. EMBO Rep. *15*, 576–585.

Zhang, X., Mofers, A., Hydbring, P., Olofsson, M.H., Guo, J., Linder, S., and D'Arcy, P. (2017). MYC is downregulated by a mitochondrial checkpoint mechanism. Oncotarget *8*, 90225–90237.

Zorova, L.D., Popkov, V.A., Plotnikov, E.Y., Silachev, D.N., Pevzner, I.B., Jankauskas, S.S., Babenko, V.A., Zorov, S.D., Balakireva, A.V., Juhaszova, M., et al. (2018). Mitochondrial membrane potential. Anal. Biochem. *552*, 50–59.

STAR★METHODS

KEY RESOURCES TABLE

REAGENT or RESOURCE	SOURCE	IDENTIFIER
Antibodies		
Caveolin-1	Cell Signaling Technology	Cat# 3267T; RRID: AB_2275453
Alexa Fluor 555-conjugated anti-rabbit IgG	Cell Signaling Technology	Cat# 4413; RRID: AB_10694110
Caspase-3	Cell Signaling Technology	Cat# 14220; RRID: AB_2798429
Phospho-p70 S6 kinase (Thr389)	Cell Signaling Technology	Cat# 9234; RRID: AB_2269803
p70 S6 kinase	Cell Signaling Technology	Cat# 2708; RRID: AB_390722
β-actin	Cell Signaling Technology	Cat# 4970; RRID: AB_2223172
Horseradish peroxidase-conjugated goat anti-rabbit IgG	Cell Signaling Technology	Cat# 7074; RRID: AB_2099233
Bacterial and virus strains		
pAAVS1-P-CAG-Tom20-CR	This paper	N/A
pLenti-EF-IRES-blast-mYF	This paper	N/A
pLenti-EF-IRES-blast-YF	This paper	N/A
pLenti-EF-IRES-blast-YF-Cav1s	This paper	N/A
pLenti-EF-IRES-blast-mActZ-FY	This paper	N/A
Chemicals, peptides, and recombinant proteins		
Dulbecco's modified Eagle's medium (DMEM)	Thermo Fisher Scientific	Cat# 11965118
Fetal bovine serum (FBS)	Thermo Fisher Scientific	Cat# 10270-106
Zell Shield	Minerva Biolabs GmbH	Cat# 13-0050
Torin 1	Merck	Cat# 475991
L-glutamine	Thermo Fisher Scientific	Cat# 25030081
Phosphate-buffered saline (PBS)	Thermo Fisher Scientific	Cat# 10010023
FuGENE HD	Promega	Cat# E2311
TransIT-2020 Reagent	TaKaRa	Cat# MIR5404
Puromycin Dihydrochloride	Thermo Fisher Scientific	Cat# A1113803
Polybrene Solution(10mg/ml)	Nacalai Tesque	Cat# 12996-81
Blasticidin S(solution)	Nacalai Tesque	Cat#03759-00
Lipofectamine RNAiMax	Thermo Fisher Scientific	Cat# 13778-030
Phenol red-free DMEM	Thermo Fisher Scientific	Cat# 31053028
Penicillin-streptomycin	Sigma-Aldrich	Cat# P4333
Rapamycin	Calbiochem	Cat# 553211-1MGCN
MitoTracker Red CMXRos	Thermo Fisher Scientific	Cat# M7513
TMRE	Thermo Fisher Scientific	Cat# T669
Formaldehyde	NEM	Cat# 3153
Glutaraldehyde	NEM	Cat# 304
Paraformaldehyde phosphate buffer solution	Wako	Cat# 163-20145
2-Deoxy-D-glucose (2-DG)	Nacalai Tesque	Cat# 10722-11
Nitrocellulose membrane	Bio-Rad	Cat# 1620115
Trypan Blue Stain	Thermo Fisher Scientific	Cat# 15250-061
InSolution™ Staurosporine, Streptomyces sp. (STS)	Merck	Cat# 569396-100UGCN
Hoechst 33342, Trihydrochloride, Trihydrate	Thermo Fisher Scientific	Cat# H1399
NP40 cell lysis buffer	Thermo Fisher Scientific	Cat# FNN0021
Protease/phosphatase inhibitor cocktail	Cell Signaling Technology	Cat# 5872
Immobilon	Millipore	Cat# WBKLS0500

(*Continued on next page*)

Continued

REAGENT or RESOURCE	SOURCE	IDENTIFIER
Bullet CBB Stain One Super	Nacalai Tesque	Cat# 13542-65
0.05% Trypsin-EDTA solution	Thermo Fisher Scientific	Cat# 25300-054
Sepazol	Nacalai Tesque	Cat# 09379-55
Primescript RT Master Mix	TaKaRa	Cat# RR036A
TB Green Premix Ex Taq II	TaKaRa	Cat# RR820A
Opti-MEM	Thermo Fisher Scientific	Cat# 11058-021
CELLBANKER	Nippon Zenyaku Kogyo	Cat# CB023
Critical commercial assays		
Q5 Site-Directed Mutagenesis Kit	New England Biolabs	Cat# E05545
In-Fusion cloning kit	TaKaRa	Cat# 639648
MitoSOX™ Red Mitochondrial Superoxide Indicator	Thermo Fisher Scientific	Cat# M36008
Protein Assay BCA Kit (Extracellular flux analysis)	Nacalai Tesque	Cat# 06385-00
The CellTiter-Glo® Luminescent Cell Viability Assay	Promega	Cat# G7570
BCA assay (Western blot analysis)	Thermo Fisher Scientific	Cat# 23227
Deposited data		
Sequence data, analysis, and resources related to the transcriptome analysis of iCMM	This paper	NCBI Sequence Read Archive (SRA) under BioProject PRJNA704503
Experimental models: Cell lines		
Human cervical adenocarcinoma HeLa cells	ATCC	CCL-2
Human hepatocellular carcinoma Hep 3B cells	ATCC	HB-8064
Human osteosarcoma U-2 OS cells	ATCC	HTB-96
Human embryonic kidney HEK293T cells	ATCC	CRL-3216
Oligonucleotides		
Control siRNA (si-Cont)	Merck	Cat# SIC001
si-DRP1	Merck	siRNA ID SASI_Hs02_00340087
Primer: Drp1 Forward: CTGTCATAAACAAGCTCCAGGAC	This paper	N/A
Primer: Drp1 Reverse: ACCAGGCTTTCTAGCACTGAG	This paper	N/A
Primer: OPA1 Forward: CGCTATCTCATACTAGGATCGGC	This paper	N/A
Primer: OPA1 Reverse: CACAATGTCAGGCACAATCC	This paper	N/A
Primer: β-Actin Forward: AGCCATGTACGTAGCCAT	This paper	N/A
Primer: β-Actin Reverse: TCTCCGGAGTCCATCACAATG	This paper	N/A
Recombinant DNA		
mYF	This paper	Addgene Plasmid Cat# 171460
YF	This paper	Addgene Plasmid Cat# 171459
YF-Cav1s	This paper	Addgene Plasmid Cat# 171462
mActZ-FY	This paper	Addgene Plasmid Cat# 171463
Tom20-CR	Miyamoto et al., 2015	Addgene Plasmid Cat# 171461
rat cytochrome b5 (ER-specific marker) -mCherry	This paper	N/A

(*Continued on next page*)

Continued

REAGENT or RESOURCE	SOURCE	IDENTIFIER
human golgin subfamily B member 1 (Golgi apparatus-specific marker)-mCherry	This paper	N/A
mCherry-human LAMP1 (Lysosome-specific marker)	This paper	N/A
Software and algorithms		
NIS-Elements AR 5.30	Nikon	https://www.nsl.nikon.com/
Fiji	Schindelin et al., 2012	https://imagej.net/Fiji
R	R Core Team 2017, 2017	https://www.R-project.org/
edgeR	McCarthy et al., 2012; Robinson et al., 2009	https://bioconductor.org/packages/release/bioc/html/edgeR.html
DAVID 6.8	NIAID/NIH	http://david.ncifcrf.gov/
python 3.7	Python software foundation	https://www.python.org/downloads/release/python-379/
NetworkX version 2.3	NetworkX developers	https://networkx.org/
Other		
3.5-cm poly-lysine-coated glass bottom dish	Matsunami	Cat# D1131H
3.2-mm sterile cloning disks	Merck	Cat# Z374431
10-cm cell culture dish	CORNING	Cat# 430167
3-kDa filters (Amicon Ultra 3K device)	Merck	Cat# UFC500324
NEPA21 electroporation	NEPAGENE	http://www.nepagene.jp/products_nepagene_0001.html
Eclipse Ti2-E microscope and Intensilight mercury-fiber illuminator	Nikon	https://www.microscope.healthcare.nikon.com/products/inverted-microscopes/eclipse-ti2-series/eclipse-ti2-e
CFP-A-Basic-NTE filter	Semrock	http://www.opto-line.co.jp/sem/detail_sets.html?pn=CFP-A-Basic
YFP-A-Basic-NTE filter	Semrock	http://www.opto-line.co.jp/sem/detail_sets.html?pn=YFP-A-Basic
mCherry-B-NTE-ZERO filter	Semrock	http://www.opto-line.co.jp/sem/detail_sets.html?pn=mCherry-C
Plan Apochromat Lambda Series, 40× objective	Nikon	https://www.microscope.healthcare.nikon.com/products/optics/cfi-plan-apochromat-lambda-series
Zyla 4.2 PLUS sCMOS camera	Oxford Instruments	https://andor.oxinst.jp/products/scmos-camera-series/zyla-4-2-scmos
A1R-HD25	Nikon	https://www.microscope.healthcare.nikon.com/products/confocal-microscopes/a1hd25-a1rhd25
SR HP Plan APO λ S 100xC Sil	Nikon	https://www.microscope.healthcare.nikon.com/selectors/objective-comparison/-1917
405, 488, and 561 laser	Nikon	https://www.microscope.healthcare.nikon.com/products/light-sources/lu-nv-laser-unit
STX stage top incubator	Tokai Hit	https://www.tokaihit.com/about-stage-top-incubator/
LightCycler 96 system	Roche Applied Science	https://lifescience.roche.com/global_en/products/lightcycler-381711.html
Synergy HTX Multi-Mode Reader	BioTek	https://www.biotek.com/products/detection-multi-mode-microplate-readers/synergy-htx-multi-mode-reader/
LUNA cell counter	Logos Biosystems	https://logosbio.com/automated-cell-counters/brightfield/luna

CellPress
OPEN ACCESS

RESOURCE AVAILABILITY

Lead contact

Further information and requests for resources and reagents should be directed to and will be fulfilled by the lead contact, Dr. Takafumi Miyamoto (takmi565@md.tsukuba.ac.jp).

Materials availability

Most of the materials used in this study are commercially available. Plasmids generated in this study have been deposited to Addgene.

Data and code availability

The article includes all data generated or analyzed during this study. All raw fastq files generated in this study are available from the NCBI Sequence Read Archive (SRA) under BioProject PRJNA704503. Original source data for Figures in the paper are available upon request to the Lead Contact author.

EXPERIMENTAL MODEL AND SUBJECT DETAILS

Cell culture and media

Human cervical adenocarcinoma HeLa cells (CCL-2), human hepatocellular carcinoma Hep 3B cells (HB-8064), and human osteosarcoma U-2 OS cells (HTB-96) were purchased from the American Type Culture Collection and were cultured in Dulbecco's modified Eagle's medium (DMEM; Thermo Fisher, 11965118) supplemented with 10% fetal bovine serum (FBS; Thermo Fisher, 10270-106) and 1% Zell Shield (Minerva Biolabs GmbH, 13-0050) at 37°C in 5% CO_2.

METHOD DETAILS

Plasmid construction

The mYF effector was produced via point mutation of EYFP by replacing Ala^{207} with Lys in the YF vector (Addgene, #20175), using the Q5 Site-Directed Mutagenesis Kit (New England Biolabs, E0554S). The YF-Cav1s effector was produced by subcloning the sequence coding aa 61–178 of human caveolin 1 (UniprotKB-Q03135) into a YF vector at the C-terminus between *Hind*III and *Sal*I. The mActZ-FY effector was produced by subcloning sequences coding aa 30–262 of codon-optimized *Listeria monocytogenes* serovar 1/2a ActA (UniprotKB-P33379) and aa 2–380 of human zyxin (UniprotKB-Q15942) into an FY vector containing the $FKBP^{F100Y}$ mutant and EYFP, at the N-terminus between the *Xho*I and *EcoR*I sites. The ActA nucleic acid sequence was optimized for mammalian cells (Nakamura et al., 2020). The Tom20-CR anchor was produced by inserting a stop codon encoding Tom20-CR (Miyamoto et al., 2015) after the *Xho*I site in the vector, using the Q5 Site-Directed Mutagenesis Kit. ER and Golgi apparatus-specific marker proteins were generated by subcloning sequences coding aa 100–134 of rat cytochrome b5 (UniprotKB-P00173) and aa 3131–3259 of human golgin subfamily B member 1 (UniprotKB-Q14789) into the mCherry vector at the C-terminus between the *EcoR*I and *Sal*I sites, respectively. To generate lysosome-specific marker proteins, the sequence coding aa 1–417 of human LAMP1 (UniprotKB-P11279) harboring V119A and L170P mutations was subcloned into the mCherry vector at the N-terminus, between the *Nhe*I and *Age*I sites. To obtain CRISPR-Cas9 expression targeting the *AAVS1* locus, donor vectors containing Tom20-CR driven by the *CAG* promoter were constructed using pAAVS1-P-CAG-mCh (Addgene, #80492). The pAAVS1-P-CAG-mCh vector was inversely amplified using primers that excluded the mCherry sequence flanked by the *EcoR*I site (termed pAAVS1-P-CAG-Tom20-CR). The insert coding Tom20-CR was amplified, followed by the assembly of the vector and insert using In-Fusion cloning kit (TaKaRa). For lentiviral expression of effector constructs, each effector was amplified and then subcloned into the *EcoR*I and *Sal*I sites of the pLenti-EF-IRES-blast vector (a gift from Yutaka Hata). All constructs were verified by sequencing following subcloning.

Transient transfection

For transient transfection of the NiCMM/iCMM system, 2.4×10^5 cells were plated on a poly-lysine-coated glass-bottom dish (Matsunami, D1131H) and incubated for 4 h at 37°C in 5% CO_2. Following incubation, the cells were transfected with the plasmid using FuGENE HD (Promega, E2311). Indicated experiments were carried out 20–32 h after transfection. For siRNA transfection, 1.4×10^5 cells were plated on a poly-lysine-coated glass-bottom dish and incubated for 4 h at 37°C in 5% CO_2. Following incubation, the cells were transfected with 10 nM of siRNA using Lipofectamine RNAiMax (Thermo Fisher Scientific, 13778-030) in accordance with the manufacturer's protocol. 24 h after the siRNA transfection, the cells were transfected with the indicated plasmids using FuGENE HD. Indicated experiments were performed 24–30 h after the plasmid transfection. All siRNAs were purchased from MERCK (control siRNA: cat# SIC001, si-DRP1: siRNA ID SASI_Hs02_00340087).

Real-time reverse-transcription polymerase chain reaction

Cells were homogenized in Sepazol, and total RNA was extracted in accordance with the manufacturer's instructions (Nacalai Tesque, 09379-55). Complementary DNA was synthesized from total RNA using Primescript RT Master Mix (TaKaRa, RR036A).

Real-time polymerase chain reactions (PCRs) were performed to amplify fragments representing the indicated messenger RNA (mRNA) expression using LightCycler 96 system (Roche Applied Science) and TB Green Premix Ex Taq II (TaKaRa, RR820A). For PCR amplification, the specific primers including 5′-CTGTCATAAACAAGCTCCAGGAC-3′ and 5′-ACCAGGCTTTCTAGCACT GAG-3′ for Drp1, 5′-CGCTATCTCATACTAGGATCGGC-3′ and 5′-CACAATGTCAGGCACAATCC-3′ for OPA1, and 5′-AGCCATG TACGTAGCCAT-3′ and 5′-TCTCCGGAGTCCATCACAATG-3′ for β-actin were used.

Lentivirus production

HEK293T cells were transiently transfected with pLenti-EF-blast vectors together with pCAG-HIVgp and pCMV-VSV-G-RSV-Rev (provided by RIKEN BRC, Ibaraki, Japan) using TransIT-2020 Reagent (TaKaRa). The medium containing lentivirus was collected.

Establishment of HeLa cells stably expressing the iCMM system

First, a HeLa cell line that stably expressed Tom20-CR was established. For gene targeting at the *AAVS1* locus, pXAT2 and pAAVS1-P-CAG-Tom20-CR were transfected into 1×10^6 cells in a single-cell suspension using NEPA21 electroporation. Two days after electroporation, 2 μg/ml of puromycin was added daily, feeding over 7 days to select for targeted cells. Serial dilution cloning was performed to isolate single-cell-derived clones. The clone was incubated with lentivirus encoding an iCMM effector in the presence of 5 μg/ml polybrene. After 48 h, the clones were cultured in the presence of 5 μg/ml blasticidin for 10 days to select for cells expressing the iCMM effector. Following the selection process, cloning was performed using 3.2-mm sterile cloning disks (Merck, Z374431).

Live-cell imaging

For epifluorescence microscopy images, ECFP, EYFP, and mCherry excitation were carried out using an Intensilight mercury-fiber illuminator (Nikon). Data were processed through a CFP-A-Basic-NTE filter (Semrock), YFP-A-Basic-NTE filter (Semrock), and mCherry-B-NTE-ZERO filter (Semrock) for ECFP, EYFP, and mCherry imaging, respectively. Cells were viewed using a 40× objective (Plan Apochromat Lambda Series, Nikon) mounted on an inverted Eclipse Ti2-E microscope (Nikon) and imaged using a Zyla 4.2 PLUS sCMOS camera (Oxford Instruments). Imaging data were processed using the NIS-Elements AR imaging software (Nikon). For confocal microscopy images, the cells were imaged using a Nikon A1R-HD25 equipped with an SR HP Plan APO λ S 100xC Sil (Nikon). A 405, a 488, and a 561 laser was used for ECFP, EYFP, mCherry excitation, respectively. All imaging experiments were completed at 37°C in 5% CO_2 using an STX stage top incubator (Tokai-Hit). For all live-cell imaging, cells were cultured in phenol red-free DMEM (Thermo Fisher, 31053028) supplemented with 10% FBS, 4 mM L-glutamine (Thermo Fisher, 25030081), and 1% penicillin-streptomycin (Sigma-Aldrich, P4333). Time was measured from the first frame, and 50 nM rapamycin (Calbiochem) was added at the indicated times. The following representative images taken by epifluorescence microscope images were processed by Clarify.ai and Denoise.ai using NIS-Elements AR 5.30: mitochondria visualized by Tom20-CR, MitoTracker Red CMXRos (Thermo Fisher, M7513), TMRE (Thermo Fisher, T669), caveolin-1 and its deletion mutants in Figure S3, organelle markers (ER, Golgi apparatus, and lysosome) in Figure S4. Confocal microscopy images were processed by Denoise.ai, and automatic deconvolution was performed with NIS-Elements AR 5.30. Notably, as the expression level of mActZ-FY was lower than that of other effectors, its fluorescence intensity was modified by changing the LUTs.

CLEM

CLEM was carried out at Japan Electron Optics Laboratory (Tokyo, Japan). Briefly, HeLa cells (cultured on a glass-bottom dish) that transiently expressed the iCMM system were washed twice with 1 ml of Phosphate buffer serin (PBS). The cells were then fixed for 10 min in a fixation mixture containing 4% formaldehyde (NEM, 3153) and 0.1% glutaraldehyde (NEM, 304) in PBS at room temperature. After three washes with PBS, the cells were imaged using a Nikon A1 plus equipped with an Apo λ S 40×C WI (Nikon), as well as a 405 and a 488 laser for ECFP and EYFP excitation, respectively. For SEM imaging, cells were subjected to post-fixation (1% OsO_4 and 1% tannic acid), Bloc contrast staining (1% uranyl acetate and lead aspartate), and dehydration, followed by Epon embedding. SEM imaging was carried out using a JSM-7900F (JEOL).

Immunocytochemistry

Cells expressing YF-Cav1s plated on a poly-lysine-coated glass-bottom dish were fixed with 4% paraformaldehyde phosphate buffer solution (Wako, 163-20145) for 10 min at 25°C, permeabilized PBS containing 0.5% Triton-100 for 15 min at 25°C, blocked in PBS containing 3% bovine serum albumin for 30 min at 25°C, stained with primary antibody against endogenous caveolin-1 (Cell Signaling, 3267T) for 16 h at 4°C, and incubated with Alexa Fluor 555-conjugated anti-rabbit IgG for 1 h at 25°C. The cells were washed three times with PBS after each step except for blocking. Imaging was performed using an Eclipse Ti2-E microscope equipped with NIS-Elements AR imaging software. The fluorescence intensity was measured by NIS-Elements AR imaging software.

Mitochondrial ROS measurement

Mitochondrial ROS was measured by MitoSOX™ Red Mitochondrial Superoxide Indicator (Thermo Fisher, M36008) according to manufactures' instruction. Briefly, cells transiently expressing NiCMM/iCMM were treated with either DMSO or 50 nM rapamycin for 2 h at 37°C in 5% CO_2. Subsequently, the cells were incubated with 5 μM MitoSOX for 10 min at 37°C in 5% CO_2, washed

with 1 ml of warmed imaging medium, then observed under an Eclipse Ti2-E microscope equipped with NIS-Elements AR imaging software. The intensity of fluorescence was analyzed by the NIS-Elements AR imaging software.

Mitochondrial membrane potential analysis

Cells were cultured for 15 min in the presence of 50 nM TMRE at 37°C in 5% CO_2. They were then washed with an imaging medium twice, and TMRE fluorescence in mitochondria was recorded with NIS software (Nikon). Fluorescence obtained from whole cell area was recorded before (F_0) and 15 min after FCCP addition (F_{FCCP}). Background fluorescence obtained from cell-free region was subtracted from both F_0 and F_{FCCP}. TMRE intensity was calculated as $F_0 - F_{FCCP}$ and normalized to the fluorescence signal recorded at 0 min.

Extracellular flux analysis

The OCR and ECAR were measured using a Seahorse XF24 extracellular flux analyzer (Seahorse Bioscience). HeLa cells stably expressing the iCMM system were seeded in a 24-well culture plate (Seahorse Bioscience) at 5×10^4 cells per well in 250 μL of culture medium and were incubated at 37 °C and 5% CO_2 for 24 h. The cells were treated with DMSO or 50 nM rapamycin for the indicated time, and the culture medium was replaced with 525 μL of XF Base Medium pH 7.4 (Seahorse Bioscience) supplemented with 4 mM GlutaMAX and 25 mM D-glucose. The cells were incubated at 37 °C in a non-CO_2 incubator for 30 min. Meanwhile, an XF24 sensor cartridge (hydrated overnight; Seahorse Bioscience) was loaded with the appropriate volumes of oligomycin (final concentration, 1 μM), protonophore FCCP (final concentration, 0.125 μM), and rotenone/antimycin A (final concentration, 0.5 μM). Three basal oxygen consumption measurements were recorded (each for 8 min) before the addition of oligomycin, FCCP, and rotenone/antimycin A. The effects of these chemicals on mitochondrial oxygen consumption were also measured three times, each for 8 min. Data were normalized to the protein concentration in each group, determined using the Protein Assay BCA Kit (Nacalai, Japan). Basal mitochondrial OCR was measured by subtracting the OCR values after treatment with rotenone/antimycin A from the initial measurements. ATP-coupled respiration (ATP production) was determined by treatment with oligomycin by subtracting oligomycin values from that corresponding to basal respiration. The maximal mitochondrial OCR was determined by subtracting the OCR after treatment with rotenone/antimycin A (as detailed above) from that measured after FCCP treatment. Basal ECAR was the initial rate measured by the extracellular flux analyzer.

ATP measurement

Intracellular ATP level was measured using The CellTiter-Glo® Luminescent Cell Viability Assay (Promega, G7570) in accordance with the manufacturer's instructions. Briefly, HeLa cells stably expressing NiCMM/iCMM were plated onto a 96-well plate. After incubation for 24 h, the cells were treated with DMSO or 50 nM rapamycin for 1 h, followed by 2-DG treatment for 4 h. Luminescence was measured using the Synergy HTX Multi-Mode Reader (BioTek).

Cell proliferation assay

Cells (1×10^6) were cultured in 10 cm culture dish for 48 h at 37°C in 5% CO_2. Trypan blue (Thermo Fisher, 15250-061) stained cells were counted using a LUNA cell counter (Logos Biosystems).

RNA-seq

Cells stably expressing the indicated iCMM system were harvested at 2 h or 6 h after rapamycin treatment, and RNA was isolated using Direct-zol 96 (Zymo Research). RNA-seq libraries were prepared from 500 ng of RNA using Quant-seq 3' FWD (Lexogen) following the manufacturer's instructions. An equal amount of each Quant-seq library was pooled and diluted to 4 pM. The library was denatured, and 2.3 nM of the denatured library was subjected to RNA-seq in an Illumina Next-seq 500 instrument using high-output flow cells and the 75 single-end mode. Using BBDuk, low-quality bases were trimmed, and poly-A or -T sequences, adapter sequences, and 11-base and one-base reads (from the left and right sides of reads, respectively) were mapped to the human genome (GRChg38.p12) using STAR-aligner (Dobin et al., 2013). Read counts were obtained using featureCounts (Liao et al., 2014). Samples that generated at least one million mapped reads were used for further analyses.

Amino acid profile analysis

Cells growing on 10-cm dishes were washed twice with ice-cold PBS, and intracellular metabolites were extracted by briefly incubating the cells with 1 ml of methanol containing internal control substances (50 μM 2-morpholinoethanesulfonic acid and 50 μM methionine sulfone) on ice. Cell debris was removed by centrifugation (14,000 × *g* for 10 min at 4°C), and 600 μl of supernatant was mixed with 300 μl of ultrapure water and 450 μl of chloroform. Following centrifugation (16,000 × *g* for 3 min at 4°C), 800 μl of supernatant was mixed with 400 μl of ultrapure water and centrifuged again. The supernatant (1 ml) was evaporated for 40 min to reduce the organic solvent content. The samples were subjected to ultrafiltration using 3-kDa filters (Amicon Ultra 3K device, Merck). After lyophilization, the samples were dissolved in 50 μl of ultrapure water. Amino acid profile analysis was conducted by LC-MS/MS (LCMS-8030, Shimadzu, Kyoto, Japan) using the primary metabolite method package version 2 (Shimadzu) according to the manufacturer's protocol.

Apoptosis analysis

Cells were treated with DMSO or rapamycin for 1 h and then incubated with 266 nM STS for 6 h. Then, the cells were incubated with Hoechst 33342 (Thermo Fisher, H1399) for 10 min for nuclear staining. After fixation with a 4% paraformaldehyde phosphate buffer solution (Wako, 163-20145), the cells were scored as possessing normal or apoptotic nuclei in several fields. Three independent experiments were conducted. Data are reported as the percentage of cells with apoptotic nuclei among total cells.

Western blot analysis

Total cell lysates were prepared using NP40 cell lysis buffer (Thermo Fisher, FNN0021) containing a protease/phosphatase inhibitor cocktail (Cell Signaling Technology, #5872), and protein concentrations were determined using a BCA assay (Thermo Fisher). For western blotting, protein samples were separated by sodium dodecyl sulfate-polyacrylamide gel electrophoresis and transferred to nitrocellulose membranes (Bio-Rad, 1620115). The membranes were blocked in Tris-buffered saline-Tween 20 containing 5% non-fat milk at room temperature for 1 h. The membranes were then incubated with the following primary antibodies for 18 h at 4°C: anti-caspase-3 (#14220), anti-phospho-p70 S6 kinase (Thr389) (#9234), anti-p70 S6 kinase (#2708), and anti-β-actin (#4970) (Cell Signaling Technology). The membranes were subsequently incubated with horseradish peroxidase-conjugated goat anti-rabbit IgG (Cell Signaling Technology) and visualized using chemiluminescence detection (Immobilon, Millipore). Coomassie brilliant blue staining was conducted using Bullet CBB Stain One Super (Nacalai, 13542-65) according to the manufacturer's protocol. Torin 1 was purchased from Merck (#475991).

QUANTIFICATION AND STATISTICAL ANALYSIS

Mitochondrial morphology analysis

Quantification of mitochondrial morphology (roundness) in Figures 1I–1K, 2D, 2E, S1D, S9D, and S9E was performed as follows: cells were cultured for 30 min in the presence of 0.5 μM MitoTracker Red CMXRos at 37°C in 5% CO_2. The cells were washed with an imaging medium twice, and the fluorescence in mitochondria was recorded using NIS software (Nikon). Fluorescence images were processed by Unsharp Mask (Power: 1.0; Area: 41) and Rolling Ball Correction using NIS-Elements AR 5.01. Subsequently, the image was processed by contrast limited adaptive histogram equalization, followed by thresholding using the open-source software Fiji (Schindelin et al., 2012). The mean value for all mitochondria' roundness in the cell was analyzed using Fiji's "Analyze Particle" function.

Transcriptome analysis

In Figures 7A–7C and S8, downstream analysis was performed using R [R Core Team (2017)]. R: A language and environment for statistical computing. R Foundation for Statistical Computing, Vienna, Austria. URL https://www.R-project.org/]. DEGs were identified using edgeR (McCarthy et al., 2012; Robinson et al., 2009). To determine DEGs, we employed a generalized linear model and the gene-wise likelihood ratio test. DEGs with fold change > 2 and FDR-adjusted $P < 0.05$ were considered significant. Competitive gene set tests were performed to account for inter-gene correlation using the camera function in the limma package as well as three-gene set collections (hallmark and C5 GO) from the Molecular Signatures Database (MSigDB) (Liberzon et al., 2011, 2015; Subramanian et al., 2005). An FDR < 0.01 was considered significant, and up to 30 gene sets in each direction (up- or downregulated) of a gene set collection were reported. If both directions occurred in two or more comparisons, the FDR was set as 1 for the different direction (for example, GO_Actomyosin was enriched in upregulated genes in mActZ, but it was also enriched in downregulated genes in other comparisons. In the plot showing upregulated genes, the FDRs for comparisons other than mActZ were 1). Functional enrichment analysis of iCMM effector-specific DEGs was performed using DAVID online tools (version DAVID 6.8; http://david.ncifcrf.gov/). Both upregulated and downregulated DEGs were included in the analysis, and a *P*-value < 0.05 was considered statistically significant.

Amino acid correlation network analysis

In Figure 7F, amino acid correlation network analysis was performed as follows:

The network graph was drawn using the Fruchterman–Reingold algorithm. This uses a force-directed graph-drawing algorithm to determine the position of each node from the relationship between the nodes and the edges. The nodes receive the force and moves. A force that brings the node closer (attractive force) and a force that moves the node away (repulsive force) work simultaneously. The attractive force f_a and the repulsive force f_r were defined by the following equations:

$$f_a = \frac{d^2}{k} \quad \text{(Equation 1)}$$

$$f_r = -\frac{k^2}{d} \quad \text{(Equation 2)}$$

$$k = C\sqrt{\frac{area}{|V|}}\, C \in \mathbb{R}, \quad \text{(Equation 3)}$$

where d was the distance between nodes, *area* was the area of the drawing space, and | V | was the number of nodes. The force applied to the node was $f_a + f_r$, and is shown in the graph below (k = 10).

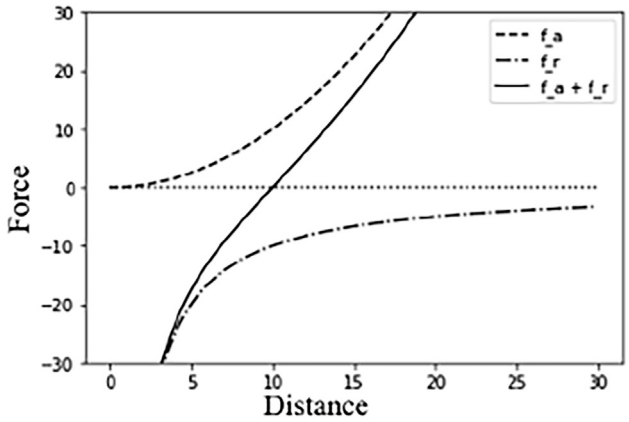

In addition, the temperature *t* that limits the amount of movement of the node was lowered step by step. The moving direction vector is given by Equation 4.

$$v = \frac{v}{|v|} * \min\left(|v|,\ t\right) \quad \text{(Equation 4)}$$

The initial position of each node was randomly assigned, the positions of the nodes were updated using the force and temperature parameters, and this calculation was repeated a certain number of times. The development environment was python 3.7, and the graph was created using NetworkX version 2.3. The edge weights were given by the correlation coefficient of each amino acid. The k value of the graph-drawing parameters of NetworkX was set to 1.5, and the other parameters used default values.

Statistical analysis

Statistical analysis was performed using R and Excel for Windows (Microsoft). Details for statistical analysis can be found in the figure legends.